

Multi-scale simulation of wave propagation and liquefaction in a one-dimensional soil column: hybrid DEM and finite-difference procedure

Matthew R. Kuhn

Received: date / Accepted: date

Abstract The paper describes a multi-phase, multi-scale rational method for modeling and predicting free-field wave propagation and the weakening and liquefaction of near-surface soils. The one-dimensional time-domain model of a soil column uses the discrete element method (DEM) to track stress and strain within a series of representative volume elements (RVEs), driven by seismic rock displacements at the column base. The RVE interactions are accomplished with a time-stepping finite-difference algorithm. The method applies Darcy's principle to resolve the momentum transfer between a soil's solid matrix and its interstitial pore fluid. Different algorithms are described for the dynamic period of seismic shaking and for the post-shaking consolidation period. The method can analyze numerous conditions and phenomena, including site-specific amplification, down-slope movement of sloping ground, dissolution or cavitation of air in the pore fluid, and drainage that is concurrent with shaking. Several refinements of the DEM are described for realistically simulating soil behavior and for solving a range of propagation and liquefaction factors, including the poromechanic stiffness of the pore fluid and the pressure-dependent drained stiffness of the grain matrix. The model is applied to four sets of well-documented centrifuge studies. The verification results are favorable and highlight the importance of the pore fluid conditions, such as the amount of dissolved air within the pore water.

Keywords liquefaction · wave propagation · DEM · pore water pressure · poromechanics

1 Introduction

Seismic wave motions propagate toward the earth's surface, where the movements and their effects are influenced by the soil through which the waves have traversed. The motions can degrade the soil, as vertical support is transferred from its granular matrix to the pore water. Soil liquefaction occurs when the inter-granular stress fades, resulting in strength loss, lateral spreading, settlement, and permanent deformation. Since the 1960s, extensive efforts have been made in understanding the mechanics of wave propagation and liquefaction, in developing predictive methods to quantify ground movements and susceptibility to liquefaction, and in developing and implementing mitigation technologies. This paper addresses the first two efforts and proposes a multi-phase, multi-scale method for the deterministic modeling and prediction of propagation and liquefaction and their effects. Such rational models are recognized as an overarching need for hazards recognition and reduction [10, 18].

Three observations illustrate the complexity of the problem. A soil becomes fully liquefied when the effective, inter-granular stress is reduced to zero and particles become disengaged from each other, becoming a suspension in two-phase flow. From the perspective of the upward moving fluid, particles appear to be tumbling downward while remaining in close proximity. From the perspective of a particle, the fluid is rushing past, creating a drag that suspends the particle and separates it from its neighbors. In either view, full liquefaction is an interaction of particles and fluid, and rational analysis requires a coupling of the two constituents' behaviors — the essence of poromechanics. Second, dense soils have a natural resistance to liquefaction, but even without fully liquefying, the particle–fluid interplay can alter fluid pressures while producing ratcheting movements of the soil mass: the phenomenon of cyclic

M. R. Kuhn
Br. Godfrey Vassallo Prof. of Engrg., Donald P. Shiley School of Engrg., Univ. of Portland, 5000 N. Willamette Blvd., Portland, OR, USA 97203 E-mail: kuhn@up.edu, ORCID 0000-0002-2971-8839.

mobility. Finally, particles and fluid interact when seismic waves pass through a soil body. But even as wave transmission changes a soil and alters its stiffness, these changes affect the transmission of seismic waves, typically slowing and diminishing the waves and changing their frequency content during the course of shaking [38,9].

The problem is clearly complex, and realistic modeling of these phenomena — whether experimentally or numerically — is exceedingly difficult. In geotechnical practice, wave propagation and liquefaction are often addressed separately: site-specific ground motions are analyzed with one-dimensional linear models [62], and the likelihood of liquefaction is assessed with empirically-based estimates of resistance and seismic demand [32]. Resolving the mutual mechanics of the two problems, an objective of the paper, has been aided by experimental studies, including the use of down-hole *in situ* instrumentation arrays [31,23] and of scaled models that are tested in geotechnical centrifuges [73,65,75]. Most common numerical methods treat soil as a continuum, requiring a constitutive model for the soil and, with some models, the fluid. The commonly used equivalent linear method assumes a linear soil model and uses a frequency-domain analysis [62,58], but the method ignores the markedly nonlinear history-dependent nature of soil stiffness and its degradation with time. With FEM simulations, a non-linear constitutive model can be assigned to the continuum [22,30], but this technique relies upon a model that is faithful to a soil's complex behavior, upon a deft choice of the model's parameters, and upon a robust algorithm that resolves the unavoidable incremental non-linearity of soil behavior. Notable recent progress has resulted from the LEAP consortium to verify and calibrate constitutive and FEM models with the use of centrifuge testing [53].

In a separate approach, the particle-by-particle DEM algorithm has been used to simulate and to explore the stress-strain and liquefaction behavior of small assemblies of particles that are subjected to cyclic loading [68,61,46]. These *element tests* provide insight into the constitutive behavior of soil, while exposing the micro-scale mechanisms that ensue during loading. Although laboratory tests are considered the primary arbiter of a soil's behavior, DEM element tests offer certain advantages in determining aspects that are less accessible in a laboratory. For example, a single DEM assembly can be reused with different loading sequences, all beginning from precisely the same particle arrangement. DEM tests also permit loading conditions of almost unlimited variety — conditions that would require different testing apparatus to be selected or constructed in a physical laboratory.

Beyond the modeling of small soil elements, the DEM has been used to directly simulate wave propagation through dry regions of intermediate size (with specimen dimensions

of a few hundred particle diameters), but only with loading frequencies of tens or hundreds of kHz, much higher than those of seismic motions [60]. When modeling larger saturated soil regions, the DEM requires a means of including both the fluid and solid phases. Recent multi-physics approaches have coupled a DEM code — used for modeling the solid particles — with a computational fluid dynamics (CFD) or atomistic-scale model to simulate the fluid phase by solving the Navier–Stokes equations, either at the macro, continuum-scale of the soil region or at the micro-scale of the pore space. Finite element and finite volume [78,20,21], smoothed particle hydrodynamics (SPH) [15], lattice Boltzmann (LBM) [19], and other methods [35] have been used in such multi-scale approaches. These coupled models have been applied to problems as diverse as fluidized beds, slurry transport, micro-scale estimation of permeability, erosion and suffusion, and liquefaction. Such multi-scale DEM/CFD methods do not require a continuum model of the solid phase, but represent the solid matrix as a system of discrete particles, while analyzing the fluid as a discretized or atomized continuum that interacts with the particles [19].

Although multi-physics methods hold promise for solving large boundary value problems, they are impeded by the size disparity between the modeled region and the soil particles themselves. The number of millimeter-size particles required to fill a region that is measured in meters can tax the capacity of available computational resources. One expedient approach uses over-sized particles that serve as proxies for particle regions [20,21], but although this approach can capture qualitative aspects of the multi-phase problem, it forfeits realistic modeling of either the fluid or the particles.

The paper concerns the problem of one-dimensional wave propagation through liquefiable soil. In the paper's multi-scale algorithm, one does not model both particles and fluid at a micro-scale. Rather, only the particles are modeled at this scale, by using the DEM algorithm to track the particles' movements and interactions, but without a CFD model to compute the fluid drag on individual particles. The pore fluid is instead reckoned at the bulk, macro-scale, by applying Darcy's principle. That is, instead of solving the Navier–Stokes equations at the micro-scale to find drag forces, we accept Darcy's equation as the gross manifestation of momentum transfer between the solid and fluid phases. As a further departure from other models [28,66], an entire region is not filled with DEM particles as one large assembly; rather, multiple small DEM assemblies are used, with each assembly representing a material point within the larger region. This approach leads to a substantial efficiency in computation. In a related approach, the DEM is combined with a continuum-based numerical method such as the FEM and material point (MPM) methods, in the so-called hierarchical multi-scale method (e.g., [29]).

The proposed algorithm uses the finite-difference method as a means of resolving the inherent non-linearity of the soil response.

The DEM algorithm, at its core, solves the equations of motion of particles, by using explicit forward-difference integration. The approach presented herein wraps the DEM algorithm within a leap-frog finite-difference approximation of the macro-scale wave equation. In this manner, the method solves the boundary value problem of vertically propagating seismic waves, driven by input displacements at a rigid base and moving through a layered soil that is being softened and possibly liquified by the motion. The problem is solved in the time domain and captures the complex behavior of the soil matrix and of the fluid flowing through it.

Other than being restricted to one dimension, the method is quite general and allows one to model and understand diverse conditions and phenomena: (1) three-dimensional motions of rock and soil, propagating as both p-waves and s-waves; (2) nearly arbitrary stress and strain paths during ground shaking; (3) sloping ground surface with down-slope movement; (4) multiple stratigraphic soil layers; (5) sub-surface water table or complete submergence of the site; (6) sloping water table with down-dip seepage forces; (7) onset and depth of liquefaction; (8) saturated soil, dry soil, or quasi-saturated soil with entrained air at a specified saturation; (9) dissolution or cavitation of entrained air; (10) effect of saturation on wave propagation and liquefaction; (11) effect of drainage that is concurrent with shaking; (12) pore fluid with a specified viscosity; (13) site-specific amplification of surface accelerations relative to those of the rock base; (14) pressure-dependence of wave speed [39] and the slowing of waves as they approach the surface; (15) dilation and the coupling of s-waves and p-waves; (16) voids redistribution and development of a water film beneath less permeable layers; (17) softening of soil during shaking, with a slowing of wave speeds and shifting of frequency content due to build-up of pore fluid pressure; (18) post-shaking consolidation and settlement; (19) post-consolidation reshaking and post-triggering behavior; and (20) relative rise of the water table during and after shaking.

Besides accounting for these diverse conditions, the method is driven by DEM models of small soil elements, allowing the retrieval of both macro- and micro-scale information, such as stress paths; fabric paths; evolution of the contact forces, coordination number, and contact network; and a soil's static strength upon subsequent reloading.

Although the method can be used to explore the phenomena listed above, most of these possibilities are well beyond the scope of the paper. The paper is restricted to a presentation of the field equations (Section 2); a description of the numerical method and issues related to its cogency

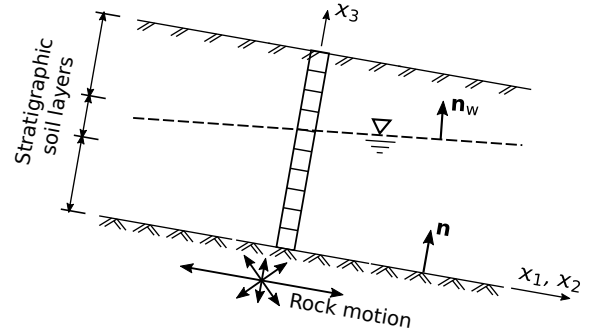


Fig. 1 One-dimensional problem of wave propagation through soil. The representative column is discretized for a soil region having multiple stratigraphic layers.

(Section 3); and the presentation of examples that provide verification with a select set of well-documented laboratory centrifuge studies (Section 4).

2 Field Equations

We analyze the one-dimensional problem of a soil column of unit area, extending from a rock base to the ground surface, with the two surfaces being parallel (Fig. 1). A rotated frame \mathbf{x} is used, in which the upward coordinate x_3 of a point \mathbf{x} is measured perpendicular to the rock and ground surfaces, with $x_3 = 0$ at the rock. Lateral x_1 and x_2 directions are parallel to the two surfaces, and, with x_3 , form an orthogonal right-hand coordinate frame. The unit normal of the rock and ground surfaces is \mathbf{n} , and the frame is aligned in unit directions \mathbf{n}_1 , \mathbf{n}_2 , and \mathbf{n}_3 , with $\mathbf{n}_3 = \mathbf{n}$. Water can be present, either below or above the ground surface, but with no perched water. When the water surface is below the ground surface, the water table can have a different slope than the ground surface; when the ground surface is submerged, the water surface is assumed horizontal. The upward normal of the water surface has unit direction \mathbf{n}_w . The soil can be comprised of multiple stratigraphic layers with interfaces that are parallel to the ground surface.

The displacement of the soil matrix $\mathbf{u}(\mathbf{x})$ has components u_1 , u_2 , and u_3 in the coordinate directions. Vector field $\mathbf{w}(\mathbf{x})$ is the displacement of the pore fluid relative to the soil matrix. The spatial gradient $\nabla_{\mathbf{x}} \mathbf{u}$ is the strain of the soil matrix, and these strains are imparted at representative volume elements (RVEs) located at material points \mathbf{x} . In the numerical implementation, an RVE is represented by a DEM assembly, and the DEM algorithm is used to compute the effective stress $\boldsymbol{\sigma}'(\mathbf{x})$ within an RVE that results from the history of strain at \mathbf{x} . In a sense, each DEM assembly is a small (numerical) laboratory specimen that interrogates the stress response of the soil matrix throughout a seismic event. The DEM algorithm has fewer limitations than most

laboratory tests, allowing nearly arbitrary stress-control or strain-control of the six components of the stress and strain tensors, allowing stress rotations, allowing control of either total or effective stresses, and permitting the modeling of conditions that are drained, undrained, or partially drained.

By applying poromechanic principles, the pore fluid pressure $p(\mathbf{x})$ at an RVE is computed from the strains of the soil matrix and of the fluid, $\nabla_{\mathbf{x}}\mathbf{u}$ and $\nabla_{\mathbf{x}}\mathbf{w}$, noting that a positive divergence $\text{div}_{\mathbf{x}}(\mathbf{w})$ represents an outflow of fluid from the RVE at \mathbf{x} . Also note that the relative displacement $\mathbf{w}(\mathbf{x})$ is that of Biot [7] and its rate $\dot{\mathbf{w}}(\mathbf{x})$ is akin to a seepage velocity, unlike the displacement \mathbf{w}' of other presentations [82], for which flux $\dot{\mathbf{w}}'(\mathbf{x})$ is associated with a discharge velocity, such that $\mathbf{w}' = n\mathbf{w}$, where n is the soil porosity.

The analysis is a direct application of the coupled Biot equations [8, 7, 82, 36], which constitute the momentum equations of the interacting solid and fluid phases,

$$\rho_{\text{g}} + \nabla_{\mathbf{x}} \cdot \boldsymbol{\sigma} = \rho \ddot{\mathbf{u}} + n\rho_{\text{f}}\ddot{\mathbf{w}} \quad (1)$$

$$\rho_{\text{f}}\mathbf{g} - \nabla_{\mathbf{x}}p - \frac{n}{k}\dot{\mathbf{w}} = \rho_{\text{f}}\ddot{\mathbf{u}} + \rho_{\text{f}}\dot{\mathbf{w}} \quad (2)$$

$$\boldsymbol{\sigma} = \boldsymbol{\sigma}' - p\mathbf{I} \quad (3)$$

where $\rho_{\text{f}}(\mathbf{x})$ is the pore fluid density; $\rho(\mathbf{x})$ is the bulk soil density, including the entrained pore fluid; $n(\mathbf{x})$ is the soil porosity; \mathbf{g} is the gravity acceleration vector, with magnitude $g = |\mathbf{g}|$; $k(\mathbf{x})$ is the soil permeability in the x_3 direction; $\boldsymbol{\sigma}(\mathbf{x})$ is the total stress, given by Eq. (3); $\boldsymbol{\sigma}'(\mathbf{x})$ is the inter-granular, effective stress; \mathbf{I} is the Kronecker tensor; and $\dot{\mathbf{w}}$ is the fluid's relative seepage velocity. Gravity \mathbf{g} is the 3-vector $[g_1, g_2, g_3]$, where g_i is defined by the inner product, $g_i = \mathbf{g} \cdot \mathbf{n}_i$.

Equations (1)–(3) neither provide nor presume a constitutive relationship between stress and strain, such that elastic, frictional, and viscous material behaviors are all consistent with the equations. The DEM assemblies furnish the constitutive relationships of the RVEs, and in its current development, the model assumes that the soil behavior is quasi-static, an assumption that is examined in Section 3.4. The equations, however, are restricted to soil with a single continuous pore fluid. If both air and water are present and both form continuous fluid networks, both flows must be accounted, requiring further refinements [26, 51].

Permeabilities are needed both above and below the water table: the air and water values, k_{a} and k_{w} . The permeability k is that of Biot, with units $\text{m}^2\text{s}^{-1}\text{Pa}^{-1}$ and which depends upon both the pore fluid and the grain matrix. The usual geotechnical hydraulic conductivity k_{G} has units of velocity m s^{-1} and is measured with water at a reference temperature. Geologists often use a permeability κ with units of m^2 or Darcies and which depends only on the grain matrix, not on the fluid. The measures are related as $k = \kappa/\mu$, $\kappa = k_{\text{G}}\mu_{\text{w,ref}}/(\rho_{\text{w,ref}}g)$, $k_{\text{w}} = \kappa/\mu_{\text{w}}$, and

$k_{\text{a}} = \kappa/\mu_{\text{a}}$, where μ_{w} and μ_{a} are the dynamic viscosities of water and air, measured in $\text{Pa}\cdot\text{s}$ [2]. The reference values at 20°C are $\mu_{\text{w,ref}} = 1.0 \text{ mPa}\cdot\text{s}$ and $\rho_{\text{w,ref}} = 998 \text{ kg/m}^3$, with g being earth's gravity. A distinction is made between $\mu_{\text{w,ref}}$ and μ_{w} , because the examples in Section 4 are from centrifuge studies in which viscosity additives were mixed with the pore water.

When restricted to the one-dimensional case, we solve the upward displacements $u_3(\mathbf{x})$ and $w_3(\mathbf{x})$ and the shearing displacements, $u_1(\mathbf{x})$ and $u_2(\mathbf{x})$, making the following assumptions

$$\sigma_{i1,1} = \sigma_{i2,2} = 0, \quad i \in \{1, 2, 3\} \quad (4)$$

$$\ddot{w}_1 = \ddot{w}_2 = 0 \quad (5)$$

where comma-separated indices in subscripts denote spatial derivatives. The second condition precludes the lateral sloshing of pore fluid through the one-dimensional soil column. An inclined water table, however, will produce lateral seepage forces within the soil column. For one-dimensional conditions, we assume that the seepage force at any depth is stationary (steady-state rather than transient), such that the quantities $p_{,1}$, $p_{,2}$, \dot{w}_1 , and \dot{w}_2 remain constant, and the lateral gradients of fluid pressure are given by the stationary vectors

$$p_{,1} = (p_{,1})_{t=0} = -\rho_{\text{f}}g(\mathbf{n}_{\text{w}} \cdot \mathbf{n}_1) \quad (6)$$

$$p_{,2} = (p_{,2})_{t=0} = -\rho_{\text{f}}g(\mathbf{n}_{\text{w}} \cdot \mathbf{n}_2) \quad (7)$$

which remain at their initial “ $t = 0$ ” values. The vertical gradient, however, will change during shaking, with the initial (pre-shaking) value given by

$$(p_{,3})_{t=0} = -\rho_{\text{f}}g(\mathbf{n}_{\text{w}} \cdot \mathbf{n}_3) \quad (8)$$

The conditions of Eqs. (6) and (8), along with Eqs. (1)–(3), establish the initial geostatic and hydrostatic (or barostatic) conditions of the RVEs. With sloping ground or a sloping water table, the geostatic stress will include a shearing stress as well as the normal σ_{33} stress.

For the case of a water table below the ground surface and the ground surface not parallel with water surface (i.e., $\mathbf{n} \neq \mathbf{n}_{\text{w}}$), the conditions are not truly one-dimensional, since a small dip-directional gradient in shearing stress is induced by the seepage force. The paper's algorithm is an approximation for this special condition.

Combining Eqs. (1)–(6) gives the four coupled differential equations of the one-dimensional problem:

$$\sigma'_{13,3} + \rho g_1 + \rho_{\text{f}}g(\mathbf{n}_{\text{w}} \cdot \mathbf{n}_1) = \rho \ddot{u}_1 \quad (9)$$

$$\sigma'_{23,3} + \rho g_2 + \rho_{\text{f}}g(\mathbf{n}_{\text{w}} \cdot \mathbf{n}_2) = \rho \ddot{u}_2 \quad (10)$$

$$\sigma'_{33,3} + \rho g_3 - p_{,3} = \rho \ddot{u}_3 + n\rho_{\text{f}}\ddot{w}_3 \quad (11)$$

$$-p_{,3} + \rho_{\text{f}}g_3 - \frac{n}{k}\dot{w}_3 = \rho_{\text{f}}\ddot{u}_3 + \rho_{\text{f}}\dot{w}_3 \quad (12)$$

in which the four kinematic variables, u_1 , u_2 , u_3 , and w_3 , are solved as functions of time. Note that the down-dip components of seepage force are included in Eqs. (9) and (10), as the quantities $\rho_f g_1 + \rho_f g(\mathbf{n}_w \cdot \mathbf{n}_1)$ and $\rho_f g_2 + \rho_f g(\mathbf{n}_w \cdot \mathbf{n}_2)$.

We will find it convenient to express the four equations in the matrix form

$$\begin{bmatrix} \rho & 0 & 0 & 0 \\ 0 & \rho & 0 & 0 \\ 0 & 0 & \rho & n\rho_f \\ 0 & 0 & \rho_f & \rho_f \end{bmatrix} \begin{bmatrix} \ddot{u}_1 \\ \ddot{u}_2 \\ \ddot{u}_3 \\ \ddot{w}_3 \end{bmatrix} = \begin{bmatrix} f_1 \\ f_2 \\ f_3 \\ f_4 \end{bmatrix} \quad (13)$$

where the stress-related quantities on the right result from the strains $\nabla_{\mathbf{x}} \mathbf{u}$ and $\nabla_{\mathbf{x}} \mathbf{w}$. These stress quantities are found with DEM simulations, as described in the next section.

For the one-dimensional problem, we enforce kinematic constraints in the transverse directions,

$$u_{1,1} = u_{1,2} = u_{2,1} = u_{2,2} = 0 \quad (14)$$

and kinematic boundary conditions also apply at the bottom of the soil column, where an input time-sequence of three-dimensional rock movements \mathbf{u} is given, and where the infiltration w_3 of fluid into or out of the rock is prohibited:

$$x_3 = 0 \Rightarrow \begin{cases} \mathbf{u}(x_3, t) = \text{given} \\ w_3(x_3, t) = 0 \end{cases} \quad (15)$$

At the soil surface, the effective stress and pore fluid pressure are zero, where fluid pressure is relative to atmospheric pressure:

$$x_3 = H \Rightarrow \begin{cases} \sigma'_{i3}(x_3, t) = 0, & i \in \{1, 2, 3\} \\ p(x_3, t) = 0 \end{cases} \quad (16)$$

The zero fluid pressure in this equation applies when the water table is below the ground surface. If the ground is submerged, fluid pressure $\rho_f g H_f$ is used instead of zero in Eq. (16₂), with H_f being the depth of submergence.

For the seismic problem, we differentiate two regimes of behavior: the dynamic period of ground shaking and the post-shaking period of consolidation. During shaking, we must consider inertial effects and apply the full Biot equations of (1), (2), and (9)–(13). The time step for the dynamic regime is limited by the Courant–Friedrichs–Lewy (CFL) condition, discussed below, which prolongs the time-driven computations.

For the post-shaking period, slow consolidation is the dominant process, and accelerations are insignificant: $\ddot{\mathbf{u}} \rightarrow 0$, $\ddot{\mathbf{w}} \rightarrow 0$. This regime was recognized by Zienkiewicz and Bettess [82], who proposed an alternative set of balance equations that involved the Laplacian of pressure, $\nabla_{\mathbf{x}}^2 p$. The author found, however, that such computations are sensitive to small perturbations of pressure, making stable computations difficult. The more straightforward approach

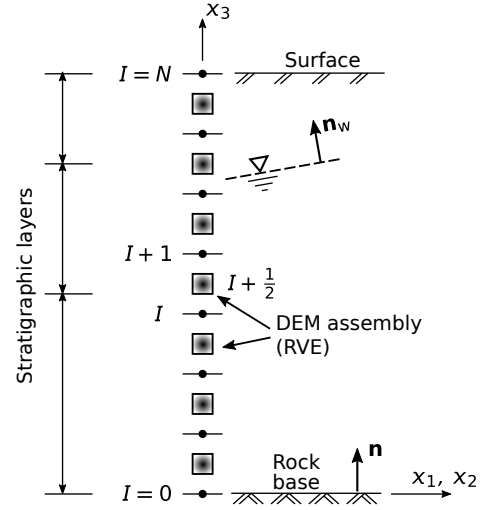


Fig. 2 Discretized soil column. Note the rotated frame, relative to that of Fig. 1.

is to reduce Eq. (12) to the following, by assuming $\ddot{\mathbf{u}} = \ddot{\mathbf{w}} = 0$:

$$\dot{w}_3 = \frac{k}{n}(-p_{,3} + \rho_f g_3) \quad (17)$$

and Eqs. (9)–(11) are reduced to the condition of constant total stresses, which remain equal to their values at the end of shaking:

$$\sigma_{13} = \text{constant}, \quad \sigma_{23} = \text{constant}, \quad \sigma_{33} = \text{constant} \quad (18)$$

These stress conditions are imposed on the DEM assemblies with a servo-algorithm and without the restriction of the CFL condition (Sections 3.2 and 3.5).

3 Numerical simulation

The soil column is discretized, as in Fig. 2. Equally spaced nodes, labeled 0 through N , are located along the soil column, between the rock base and the ground surface. The initial spacing is Δx , such that node I is located at coordinate $x_3^I = I\Delta x$ above the base, with initial lateral coordinates $x_1^I = x_2^I = 0$. The N RVEs, modeled with DEM assemblies, are labeled $\frac{1}{2}, 1\frac{1}{2}, \dots, N - \frac{1}{2}$ and are located midway between adjacent nodes, with RVE $I + \frac{1}{2}$ located above node I , at coordinate $x_3^{I+\frac{1}{2}} = (I + \frac{1}{2})\Delta x$, for $I = 0$ through $N - 1$. Both the nodes and the RVEs are material points, and they will move and deform with the soil column. As such, the spacing Δx between two nodes can change during the simulation.

To track possibly large strains, the deformation of the soil matrix of RVE $I + \frac{1}{2}$ is measured with its deformation gradient, $F_{ij}^{I+\frac{1}{2}} = \delta_{ij} + \partial u_i / \partial X_j$, where \mathbf{X} is a point's original location in the vicinity of RVE $I + \frac{1}{2}$. The determinant

$\det(\mathbf{F})$ is the current volume of the soil matrix relative to the original volume. The total fluid deformation gradient \mathbf{W} at $x^{I+\frac{1}{2}}$ is $W_{ij}^{I+\frac{1}{2}} = \delta_{ij} + \partial u_i^{I+\frac{1}{2}} / \partial X_j + \partial w_i^{I+\frac{1}{2}} / \partial X_j$, remembering that \mathbf{w} is the fluid displacement relative to the displacement \mathbf{u} of the grain matrix. The difference $\det(\mathbf{W}) - \det(\mathbf{F})$ is the volume of fluid outflow per unit of original fluid volume, and $\det(\mathbf{F})/\det(\mathbf{W})$ is the ratio of the current and original void volumes within the grain matrix.

The soil column can have multiple stratigraphic layers, with each layer assigned its own density, grain-size distribution, fabric, permeability, and saturation. A DEM assembly must be created for each RVE, having the characteristics of the stratigraphic layer within which the RVE resides. As a practical expedient, we start with a single progenitor DEM assembly for each stratigraphic layer, having the same density, grain-size distribution, and fabric as the layer's soil. Each of these progenitor assemblies is then consolidated (either with compression or with expansion, and either isotropically or anisotropically) while, in the case of sloping ground, simultaneously increasing the shearing stress, thus creating the proper initial stress conditions at each RVE depth. In this manner, one can create assemblies for all of the RVE points from a few progenitor DEM assemblies, assuring the proper initial geostatic and hydrostatic conditions at each RVE.

The water table can be located either below or above the ground surface. The DEM model must account for the stiffness of the pore fluid, and in the model's current development, the pore fluid can be either water with 100% saturation, entirely air with 0% saturation, or quasi-saturated water. In the latter condition, air is in the form of entrapped and isolated bubbles within the water, usually found at saturations greater than 90% [24]. The model accounts for changes in bubble size that result from changes in the pore fluid pressure, and the model also allows for the dissolution of gaseous air when the pressure increases and for the emergence (cavitation, disgoring) of gaseous air when the pressure decreases in a fluid that is already saturated with dissolved air [25]. The model also makes allowance for the formation of water vapor when water pressure is reduced to the vapor pressure [54]. In the model's current development, however, field equations (1) and (2) permit only a single continuous pore fluid, and further refinement would be needed when more than one fluid phase is continuous (e.g., petroleum extraction in which three continuous phases of oil, water, and gas can be present).

The model differs from multi-physics models in which a DEM assembly of particles is coupled with a CFD (computational fluid mechanics) model of the fluid (e.g., [20, 15]). Instead, each DEM assembly incorporates a poromechanic representation of the pore fluid, which supplies the relationship between pore fluid pressure p and fluid strain.

In DEM simulations, the grain bodies are geometric objects that interact in a pairwise manner, and the forces between grains, typically at their contacts, collectively comprise the average inter-granular, effective stress of the assembly, σ' . The effective stress is computed in the established manner [5], as a double-sum over the N^p particles q , and over the M^q contacts c of the particle q ,

$$\sigma'_{ij} = \frac{1}{V} \sum_{q=1}^{N^p} \sum_{c=1}^{M^q} r_i^{c,q} f_j^{c,q} \quad (19)$$

where $\mathbf{r}^{c,q}$ is the vector from the center of q to the contact c , $\mathbf{f}^{c,q}$ is the contact force acting on q , V is the assembly's volume, and tensile stress is positive. The equation permits particles of arbitrary shape and accounts for multiple contacts between a pair of particles [5]. Equation (19) is commonly used in DEM studies that explore the stress evolution and constitutive behavior of granular materials [6, 76, 43].

Although most DEM liquefaction studies impose a constant-volume constraint to approximate undrained conditions [68, 61, 46], the model herein relies upon partial-drainage and requires calculation of pore fluid pressures. The fluid, whether a liquid, gas, or mixture, requires a poroelastic representation that gives the relationship among the matrix strain, fluid outflow, and fluid pressure. For saturated or quasi-saturated water, the relationship is

$$\begin{aligned} p = p_o &+ \left\{ -\det(\mathbf{F}) + (1 - n_o) \left[1 + (\sigma'_{kk} - \sigma'_{o,kk}) / (3K_s) \right] \right. \\ &\quad \left. + n_o(1 - \beta)S_o + n_o(1 - \beta)N_o\pi D^3/6 \right\} \\ &\quad / \left[(1 - n_o)/K_s + n_o(1 - \beta)S_o/K_w \right] \end{aligned} \quad (20)$$

which is based on well-established physical parameters of the grains and pore fluid. By applying this relationship, the model captures the effect of initial saturation S_o on liquefaction resistance, which can be significant [79, 80]. In the equation, n_o , σ'_o , and p_o are the initial porosity, effective stress, and fluid pressure in the reference state; K_s and K_w are the bulk moduli of the solid grains and of liquid water; D is a representative diameter of gas bubbles, assumed uniform; N_o is the number of bubbles per unit of original void volume; and β is the outflow of pore fluid, $\det(\mathbf{W}) - \det(\mathbf{F})$, per volume of pore fluid (see [8, 36, 45], noting that $\beta = -\zeta$ in the author's previous work). For the one-dimensional model, β is the vertical outflow of pore fluid relative to the moving soil matrix, $\beta = dw_3/dx_3$. To account for changes in bubble volume, one must also consider the gas-water surface tension and the gas solubility and water vapor pressure, and one is referred to [45].

The air in a dry soil is also treated as a fluid, with its own density, compressibility, and permeability. The relationship between air outflow w and pressure p is derived in the Appendix.

3.1 Dynamic regime

The field equations (9)–(12) are numerically integrated in a series of time-steps Δt , also called *episodes*. The displacements \mathbf{u} and \mathbf{w} in each episode are used for determining the gradients (strains), $\partial u_i / \partial x_3$ and $\partial w_3 / \partial x_3$, which are then imposed upon the DEM assemblies to determine the resulting stresses, noting that subscript “ i ” refers to the set of directions, $i \in \{1, 2, 3\}$. The gradients of the stresses are then used in Eqs. (9)–(12) to solve the next displacements of the nodes. As such, these equations are applied in a step-wise repetitive manner throughout the shaking event, with the entire process driven by the prescribed rigid rock motion. As in Eq. (15), the three-dimensional rock displacements $\mathbf{u}^0(t)$ at node 0 are discretized as a series of $M + 1$ three-dimensional displacements, $u_i^0, u_i^{0,1}, \dots, u_i^{0,J}, \dots, u_i^{0,M}$, separated by a common interval Δt , at times $t = 0, t_1, \dots, t_J, \dots, t_M$, with $t_J = J\Delta t$. The final time t_M is at the end of shaking, $t_{\text{end,shaking}}$. The rock base is assumed impervious, so that $w_3^{0,J} = 0$ throughout the simulation.

With the central-difference algorithm that is used for the dynamic regime, velocities are computed mid-step, $\dot{u}_i^{I,J+\frac{1}{2}}$ and $\dot{w}_3^{I,J+\frac{1}{2}}$, at time $t_{J+\frac{1}{2}}$ for each node I . Note that when two superscripts are used, separated by a comma, the first index refers to positions along the height of the soil column, and the second index refers to time. Stress and pressure are measured at the RVEs and denoted as $\sigma_{i3}^{I+\frac{1}{2},J}$ and $p^{I+\frac{1}{2},J}$; the gradients of stress and pressure are computed at the nodes, as $\sigma'_{i3,3}^{I,J}$ and $p'_{,3}^{I,J}$; and deformations are computed at the RVEs, as $u_{i,3}^{I+\frac{1}{2},J}$ and $w_{3,3}^{I+\frac{1}{2},J}$.

The episode Δt is limited by the Courant–Friedrichs–Lewy condition, described below. We distinguish, however, between episode Δt used for the nodal motions and the time-steps that are used within the DEM algorithm that imparts the RVE deformations and computes the resulting stresses. For each DEM assembly, multiple DEM time-steps can occur within Δt , with the DEM steps being sufficiently small to produce quasi-static deformation. This and other matters related to temporal and rate effects are addressed in Section 3.4.

Prior to shaking, the DEM assemblies are consolidated to the imposed geostatic and hydrostatic stresses and pressures, and they are allowed to equilibrate under these conditions (see text following Eq. 8). The pore fluid characteris-

tics k , S_o , K_w , n_o , N_o , and D in Eq. (20) are then assigned before shaking commences.

Figure 3 shows a schematic of the dynamic algorithm for computing the displacements $u_i^{I,J+1}$ and $w_3^{I,J+1}$ at the next time t_{J+1} , with arrows representing dependencies within the algorithm. The algorithm is summarized in Fig. 4.

The accelerations in Eqs. (9)–(12) and the relative flow velocity \dot{w}_3 in Eq. (12) are estimated from the mid-step velocities:

$$\ddot{u}_i^{I,J} \approx \frac{1}{\Delta t} \left(\dot{u}_i^{I,J+\frac{1}{2}} - \dot{u}_i^{I,J-\frac{1}{2}} \right), \quad i \in \{1, 2, 3\} \quad (21)$$

$$\ddot{w}_3^{I,J} \approx \frac{1}{\Delta t} \left(\dot{w}_3^{I,J+\frac{1}{2}} - \dot{w}_3^{I,J-\frac{1}{2}} \right) \quad (22)$$

$$\dot{w}_3^{I,J} \approx \frac{1}{2} \left(\dot{w}_3^{I,J+\frac{1}{2}} + \dot{w}_3^{I,J-\frac{1}{2}} \right) \quad (23)$$

With these estimates, Eqs. (9)–(12) give the mid-step velocities at time $t_{J+\frac{1}{2}}$, as the four unknown values in matrix equation

$$([A_1] + [A_2]) \begin{bmatrix} \dot{u}_1^{I,J+\frac{1}{2}} \\ \dot{u}_2^{I,J+\frac{1}{2}} \\ \dot{u}_3^{I,J+\frac{1}{2}} \\ \dot{w}_3^{I,J+\frac{1}{2}} \end{bmatrix} = [a] \quad (24)$$

where

$$[A_1] = \begin{bmatrix} \rho & 0 & 0 & 0 \\ 0 & \rho & 0 & 0 \\ 0 & 0 & \rho & n\rho_f \\ 0 & 0 & \rho_f & \rho_f \end{bmatrix}, \quad [A_2] = \begin{bmatrix} 0 & 0 & 0 & 0 \\ 0 & 0 & 0 & 0 \\ 0 & 0 & 0 & 0 \\ 0 & 0 & 0 & \frac{n\Delta t}{2k} \end{bmatrix} \quad (25)$$

$$[a] = \Delta t \begin{bmatrix} \sigma'_{13,3}^{I,J} + \rho g_1 + \rho_f g (\mathbf{n}_w \cdot \mathbf{n}_1) \\ \sigma'_{23,3}^{I,J} + \rho g_2 + \rho_f g (\mathbf{n}_w \cdot \mathbf{n}_1) \\ \sigma'_{33,3}^{I,J} + \rho g_3 - p'_{,3}^{I,J} \\ -\frac{n}{2k} \dot{w}_3^{I,J-\frac{1}{2}} + \rho_f g_3 - p'_{,3}^{I,J} \end{bmatrix} + [A_1] \begin{bmatrix} \dot{u}_1^{I,J-\frac{1}{2}} \\ \dot{u}_2^{I,J-\frac{1}{2}} \\ \dot{u}_3^{I,J-\frac{1}{2}} \\ \dot{w}_3^{I,J-\frac{1}{2}} \end{bmatrix} \quad (26)$$

In the last equation, the gradients of stress and pressure (at nodes 1 through $N - 1$) are approximated as

$$\sigma'_{i3,3}^{I,J} \approx \frac{1}{\Delta x} \left(\sigma_{i3}^{I+\frac{1}{2},J} - \sigma_{i3}^{I-\frac{1}{2},J} \right), \quad i \in \{1, 2, 3\} \quad (27)$$

$$p'_{,3}^{I,J} \approx \frac{1}{\Delta x} \left(p^{I+\frac{1}{2},J} - p^{I-\frac{1}{2},J} \right) \quad (28)$$

The shaking process is driven by the input displacements, $u_i^{0,J}$, of the rigid (reflecting) base, with fluid infiltration $w_3^{0,J}$ equal to zero (i.e., the boundary conditions of Eq. 15). At the ground surface, stress and pressure are zero, as in Eq. (16), which is enforced by using the following gradients at node N ,

$$\sigma'_{i3,3}^{N,J} \approx \frac{2}{\Delta x} \left(-\sigma_{i3}^{N-\frac{1}{2},J} \right), \quad i \in \{1, 2, 3\} \quad (29)$$

$$p'_{,3}^{N,J} \approx \frac{2}{\Delta x} \left(-p^{N-\frac{1}{2},J} \right) \quad (30)$$

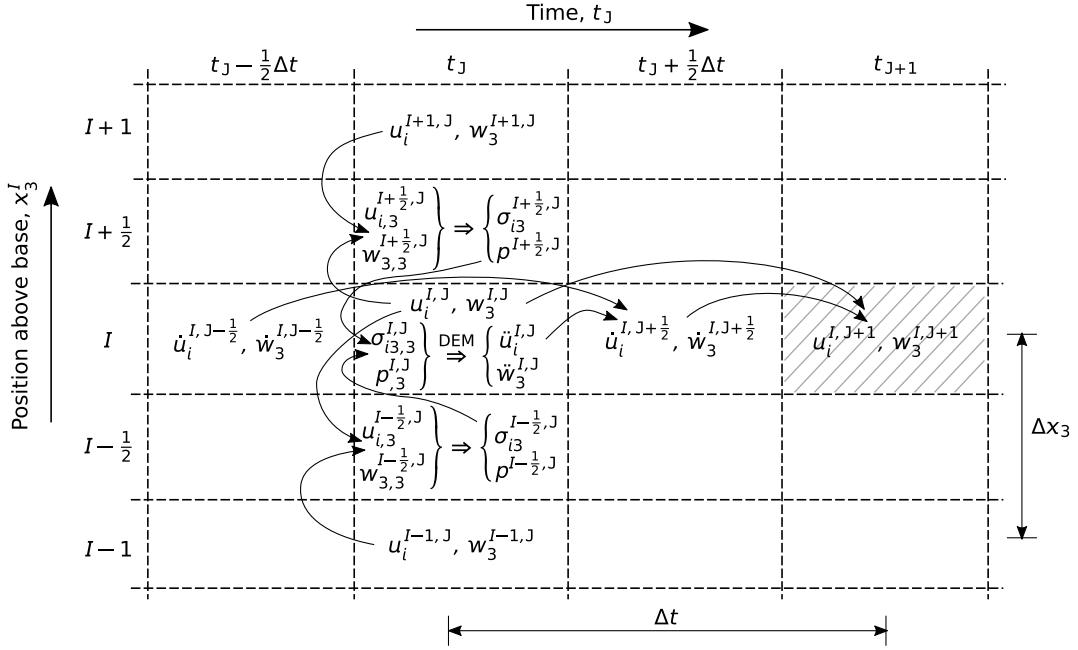


Fig. 3 Schematic (stencil) of relationships among discretized quantities. Arrows show the dependencies of quantities in computing the displacements, u_i and w_3 , for the next, $J + 1$, time step (hatched).

Equation (24) is solved for the mid-step velocities, which are used for finding the next displacements,

$$u_i^{I,J+1} = u_i^{I,J} + \Delta t \cdot \dot{u}_i^{I,J+\frac{1}{2}}, \quad i \in \{1, 2, 3\} \quad (31)$$

$$w_3^{I,J+1} = w_3^{I,J} + \Delta t \cdot \dot{w}_3^{I,J+\frac{1}{2}} \quad (32)$$

and the nodal coordinates are updated to equal their original coordinates plus the accumulated displacements:

$$x_i^{I,J+1} = x_i^{I,0} + u_i^{I,J+1}, \quad i \in \{1, 2, 3\} \quad (33)$$

Note that the accumulated relative fluid displacement $w_3(\mathbf{x})$ represents a migration of water through the soil column (positive w_3 being upward), which will cause the water table to rise or fall. The x_3 height of the water table above the base equals the original height plus the sum of displacements, $u_3 + w_3$. If the water table is located between two nodes, the displaced height of the water table is found by interpolating between the new heights (Eq. 33) of the two nodes, those above and below the table.

Once the new nodal displacements are solved at t_{J+1} with Eqs. (31)–(32), the new cumulative strains are estimated at the RVEs (here, we replace time $J + 1$ with J):

$$u_{i,3}^{I+\frac{1}{2},J} \approx \frac{1}{\Delta x} \left(u_i^{I+\frac{1}{2},J} - u_i^{I-\frac{1}{2},J} \right), \quad i \in \{1, 2, 3\} \quad (34)$$

$$w_{3,3}^{I+\frac{1}{2},J} \approx \frac{1}{\Delta x} \left(w_3^{I+\frac{1}{2},J} - w_3^{I-\frac{1}{2},J} \right) \quad (35)$$

The differences between these strains and the previous strains are the increments that are imposed upon the DEM

assemblies in next episode Δt , and the DEM algorithm is used to compute the resulting stresses and pressures for this integration step. Note that the DEM assemblies are subject to full strain-control during the dynamic regime: the accumulated large-strain deformations gradients F_{i3} and W_{33} are determined from Eq. (34)–(35) and imposed on the assemblies, while deformation constraints are also enforced on the one-dimensional system, as $F_{11} = F_{22} = 1$ and $F_{12} = F_{21} = F_{31} = F_{32} = 0$.

Because the dynamic problem solves a wave equation, increment Δt must be sufficiently small so that the solution does not outpace the wave equation's characteristic velocities. The Courant–Friedrichs–Lewy (CFL) condition requires the Courant number, $C = c\Delta t/\Delta x$, is less than 1, where c is the characteristic wave speed. After initial consolidation but before shaking, various moduli Q are measured with small strain-probes so that the corresponding wave speeds can be estimated. The moduli include the shear moduli in the x_1 and x_2 directions, the drained uniaxial confined compression modulus, and the undrained (Biot's closed system) uniaxial confined compression modulus. The largest of these moduli among all RVEs is used to estimate the fastest (local) wave speed $\sqrt{Q/\rho}$, which is used to compute the increment Δt for all RVEs. In the simulations of this paper, a C of 0.4 was used. The small strain-probes will change a DEM assembly's fabric, so one must restore each assembly to its original consolidation condition before beginning the shaking simulation.


```

1 Consolidate the DEM assemblies to their geostatic conditions
2 Set fluid properties
3 Run DEM to find wave speeds. Set  $\Delta t = C\Delta x/c$ , with  $C \approx 0.2$ 
4 Read input rock motions  $\mathbf{u}(t)$  at  $x_3 = 0$ ,  $t = 0 \dots t_{\text{end\_shaking}}$ 
5 Set  $t \leftarrow 0$ ,  $J \leftarrow 0$ 
6 Set  $u_i^{I,J} \leftarrow 0$ ,  $w_3^{I,J} \leftarrow 0$ ,  $i \in \{1, 2, 3\}$ ,  $I \in \{0 \dots N\}$ 
7 while  $t < t_{\text{end\_shaking}}$  do
8   Find rock displacements,  $u_i^{0,J}$ ,  $i \in \{1, 2, 3\}$ 
9   Find strains,  $u_{i,3}^{I+\frac{1}{2}} & w_{3,3}^{I+\frac{1}{2}}$ ,  $i \in \{1, 2, 3\}$ ,  $I \in \{0 \dots N-1\}$ . Eqs. (34–35)
10  Run DEM to find  $\sigma'_{i3}^{I+\frac{1}{2},J} & p^{I+\frac{1}{2},J}$ ,  $i \in \{1, 2, 3\}$ ,  $I \in \{0 \dots N-1\}$ 
11  Find gradients,  $\sigma'_{i3,3}^{I,J} & p_{,3}^{I,J}$ ,  $i \in \{1, 2, 3\}$ ,  $I \in \{1 \dots N\}$ . Eqs. (27–30)
12  Find velocities,  $u_i^{I,J+\frac{1}{2}} & w_3^{I,J+\frac{1}{2}}$ ,  $i \in \{1, 2, 3\}$ ,  $I \in \{1 \dots N\}$ . Eq. (24)
13  Update displacements,  $u_i^{I,J+1} & w_3^{I,J+1}$ ,  $i \in \{1, 2, 3\}$ ,  $I \in \{1 \dots N\}$ . Eqs. (31–32)
14  Update node locations,  $x_i^{I,J+1}$ ,  $i \in \{1, 2, 3\}$ ,  $I \in \{1 \dots N\}$ . Eq. (33)
15  Update water table height
16   $J \leftarrow J + 1$ 
17   $t \leftarrow t + \Delta t$ 
18 end

```

Fig. 4 Algorithm for the dynamic regime of ground shaking.

3.2 Post-shaking consolidation regime

Ground shaking causes fluid pressure to change within the soil column, and the shaking is followed by a quiescent period of consolidation during which pressure is redistributed within the column and eventually equilibrates to the hydrostatic (or barostatic) condition. During this consolidation, excess fluid pressure is dissipated, causing the ground to settle. The process is slow, but because consolidation is not controlled by wave speed, the process is not limited by the CFL condition, allowing a larger step Δt . The numerical method is a finite difference solution of Terzaghi's one-dimensional consolidation theory, with the DEM assemblies supplying the soil's stiffnesses [74].

The post-shaking algorithm is summarized in Fig. 5. It begins with the nodal positions and with the full internal information of each DEM assembly (contact forces, particle positions, etc.) that were left at the end of the dynamic algorithm. (As a practical matter, the rock must come to rest, with zero velocity, at the end of shaking, due to the lack of inertia terms in the post-shaking consolidation equations.)

The consolidation process is governed by Eq. (17), which is applied in each time-step to determine the upward pore fluid displacement w_3 of the next step. A forward-difference algorithm is used:

$$w_3^{I,J+1} \approx w_3^{I,J} + \Delta t \frac{k}{n} \left(-p_{,3}^{I,J} + \rho_f g_3 \right) \quad (36)$$

where the gradient $p_{,3}^{I,J}$ is estimated with Eqs. (28) and (30). The new displacements $w_3^{I,J+1}$ are then used to compute the fluid strains with Eq. (35), and these strains become input for the DEM assemblies. When applying the fluid strains, the vertical total stresses and the horizontal shearing

stresses, $\sigma_{i3}^{I,J}$, are maintained constant (i.e., Eq. 18) by using a DEM servo-algorithm, while also maintaining one-dimensional conditions of the soil column: $\sigma_{i3} = \text{constant}$, $F_{11} = F_{22} = 1$ and $F_{12} = F_{21} = F_{31} = F_{32} = 0$.

In the dynamic algorithm of the previous section, displacements $u_i^{I,J}$ and $w_3^{I,J}$ were determined and the corresponding strains $u_{i,3}^{I+\frac{1}{2},J}$ were applied to the DEM assemblies (Eqs. 31, 32, 34, and 35). For post-shaking consolidation, only the fluid displacements of Eq. (36) are imposed. The DEM servo-algorithm maintains constant total stress, as in Eq. (18), by deforming the grain skeleton and adjusting the fluid pressure. The gradients of the resulting pressures are used in Eq. (36) in the next step, and the resulting DEM deformations $F_{i3}^{I+\frac{1}{2},J+1}$ are integrated, starting at the base, to find the new node displacements:

$$u_i^{I,J+1} = u_i^{I,0} + \sum_{K=1}^I \left(F_{i3}^{K+\frac{1}{2},J+1} - \delta_{i3} \right) \Delta x \quad (37)$$

Because increment Δt is not constrained by the CFL criterion during consolidation, Δt can be stretched, so that the strain rates within the DEM assemblies are larger than those of the dynamic algorithm. The rates, however, must not be so fast that the quasi-static balance of forces among particles is compromised. In the current implementation, Δt is stretched so that strains within the assemblies are advanced in increments of about 1×10^{-6} .

3.3 Spatial increment

The spacial increment Δx brings subtle choices to the coding. The balance equations (1)–(2) and (9)–(13) are based

```

1  Retrieve DEM information from the end of dynamic shaking
2   $t \leftarrow t_{\text{end\_shaking}}$ 
3   $u_i^{I,J}$  and  $w_3^{I,J} \leftarrow$  inherited from the end of shaking
4  while  $t < t_{\text{end\_consolidation}}$  do
5      Find fluid strains,  $w_{3,3}^{I+\frac{1}{2},J}$ ,  $I \in \{1 \dots N-1\}$ . Eq. (35)
6      Run DEM to find strains  $F_{i3}^{I+\frac{1}{2},J}$ ,  $I \in \{1 \dots N-1\}$ 
7      Find pressure gradients,  $p_{,3}^{I,J}$ ,  $I \in \{1 \dots N\}$ . Eqs. (28,30)
8      Find fluid displacements,  $w_3^{I,J+1}$ ,  $I \in \{1 \dots N\}$ . Eq. (36)
9      Update node displacement,  $u_i^{I,J+1}$ ,  $I \in \{1 \dots N\}$ . Eq. (37)
10     Update node locations,  $x_i^{I,J+1}$ ,  $i \in \{1, 2, 3\}$ ,  $I \in \{1 \dots N\}$ . Eq. (33)
11     Update water table height
12      $J \leftarrow J + 1$ 
13      $t \leftarrow t + \Delta t$ 
14 end

```

Fig. 5 Algorithm for the post-shaking consolidation regime.

on the Cauchy stress σ , and the stress gradients are with respect to the current (deformed) positions \mathbf{x} . (Different balance equations would apply, if the Piola stress was adopted.) Therefore, the DEM code should return the Cauchy stress, as is done with Eq. (19), provided that $\mathbf{r}^{c,q}$ and $\mathbf{f}^{c,q}$ are measured in an assembly's deformed configuration. The stress gradients in Eqs. (27)–(30) should also be computed with increments Δx in the current, displaced nodal positions of Eq. (33).

Spatial increment Δx in Eqs. (34), (35), and (37) depends upon the choice of the kinematic description of strain. In the author's DEM code, the deformation of an assembly is referenced with the large-strain deformation gradient \mathbf{F} , the gradient of the current position with respect to the undeformed configuration. As such, the original spacing Δx is used in Eqs. (34), (35), and (37).

3.4 Uniform and quasi-static loading

This section addresses three underlying assumptions of the model and its current implementation: (1) wavelengths during seismic loading and their relation to the assumed uniformity of strain within the RVEs; (2) the possible effect of strain gradients within the RVEs; and (3) the quasi-static assumption and the choice of a time step for the DEM simulations. Symbol f will represent the frequency of rock motion; c is a generic wave velocity (s-waves or p-waves); and γ is the corresponding strain $u_{i,3}$.

In the DEM algorithm, strain is assumed uniform at the meso-scale of an assembly's dimensions. Seismic wavelengths can be approximated as c/f , and for typical s-wave speeds and for frequencies less than 100 Hz, the wavelengths are comparable to a column's height (perhaps meters or tens of meters). These wavelengths are far greater than the dimensions of the DEM assemblies or than the sizes of the particles' themselves (in the examples of Sec-

tion 4, the assemblies are about 3 mm tall and the particle size is about 0.19 mm). Even as the material approaches liquefaction and wave speed is reduced, the wavelength will greatly exceed the particles' size. As such, strain can be applied to a DEM assembly (steps 9 and 10 of Fig. 4), knowing that this strain is nearly uniform within an assembly's dimensions.

A possible concern, however, is raised by a finding of the author that the stress response of a granular material intrinsically depends on the gradient of strain as well as on the strain itself, a possible source of wave scattering [40]. One must consider whether the macro-scale gradient of strain within the soil column can influence the local RVE response, an effect that appears when the dimensionless ratio $D_{50}(\partial\gamma/\partial x_3)/\gamma$ exceeds 0.1 [40]. Assuming harmonic motion in a one-dimensional medium of infinite length, the ratio during wave propagation is approximately $2D_{50}\pi f/c$. For frequencies less than 100 Hz and for typical p-wave speeds, the ratio $D_{50}(\partial\gamma/\partial x_3)/\gamma$ is about 0.0001 (at the higher frequencies of 50g centrifuge testing, about 0.005), which is much less than 0.1 and indicates that strain-gradients do not need to be considered in the RVE response.

The DEM model used herein presupposes an RVE response that is quasi-static and rate-independent, since a significant computational speed-up can be exploited when this assumption applies. The assumption can be verified by measuring the dimensionless inertial number I , defined as $I = \dot{\gamma}d\sqrt{\rho_s/\bar{p}}$ [16]. The number is used with granular materials to distinguish between slow flows, in which contacts are enduring, and rapid collisional flows, in which contacts are brief and particle motions are dominated by inertia transfers. In the definition, d is the particle size, $\dot{\gamma}$ is the strain rate, ρ_s is the density of the particles, and \bar{p} is the mean effective stress (also called the particle pressure within the granular rheology community). The author uses a related dimensionless quantity, $\dot{\gamma}\sqrt{k_n/m}$, where k_n is the normal stiffness between two contacting particles, and

m is the particle mass [71]. This quantity is the ratio of the shearing rate and the rate at which force-information is transferred through the material (i.e., wave velocity). For dry granular materials, a small value of either quantity indicates a quasi-static condition, in which behavior is rate-independent; whereas, large values indicate a collisional viscous domain. Quasi-static conditions are found to apply when $I < 0.001$; whereas, collisional behavior applies when $I > 0.2$ [16]. At intermediate, transitional values, a granular material behaves as a shear-thickening viscous material. Throughout the simulations of Section 4, the inertial number was consistently in the quasi-static range, with values less than 0.00006 for dry soil, less than 0.00001 for non-liquefying saturated soil, and less than 0.001 for liquefied saturated soil. The values were usually much smaller, and the largest values were only attained during brief, transitory moments. Such shear rates are well within the range of quasi-static behavior [34, 77].

Knowing that the macro-scale problem is quasi-static, one can reduce the DEM computation time, by choosing a DEM time-step and/or a DEM particle mass m that gives a smaller value of $\dot{\gamma}\sqrt{k_n/m}$, thus maintaining numerical stability with a speed-up of simulation time [57, 71], a technique that is commonly used in quasi-static DEM simulations [76, 43].

3.5 DEM necessities

Soil behavior in the one-dimensional column is interrogated and measured with N three-dimensional DEM assemblies, located at the RVE points. The shaking imposes an extended deformation narrative for each assembly, a narrative that is divided into a sequence of M short deformation episodes of duration Δt . Each DEM episode is simulated by dividing the strain increment during Δt into multiple DEM time steps, so that a nearly uniform DEM strain rate is applied among all N assemblies and within all M episodes Δt . A nearly uniform DEM strain rate is desired because the DEM simulations, although they are nearly quasi-static and rate-independent across one or two orders of magnitude of strain rate, can exhibit a slight rate-dependence for larger disparities of the rate [59]. In the current implementation, the DEM algorithm advances the strain in increments of between 1×10^{-7} and 1×10^{-6} per DEM time-step. Although this range is maintained for each DEM assembly, the number of DEM time-steps varies among assemblies, so that each assembly's full strain increment is attained in the Δt episode.

When the simulation of ground shaking and consolidation is finished, one can retrieve a full account of the stress-strain-fabric evolution at each RVE for its entire history of motion. A realistic simulation, however, requires four DEM features, features that are not included in most

DEM codes: a poromechanic component, a robust and general servo-algorithm, a contact model that yields a proper increase of soil stiffness with depth, and a contact model that is energetically consistent.

As previously discussed, the DEM code must include poromechanic models for all pore fluids that are present in the soil column. The model must account for the coupling of the inter-granular effective stress, pore fluid pressure, strain of the soil matrix, and strain of the pore fluid. The solution in [45] models water-saturated and quasi-saturated soils. The model for dry soil is derived in the Appendix.

Several combinations of stress-control and strain-control are required within the dynamic and consolidation regimes: the dynamic algorithm imposes full strain-control; the consolidation algorithm requires control of three of the six stress components; and the pre-processing of initial assembly consolidation and measurement of elastic moduli require other forms of stress-control. With consolidation, total stress is controlled; whereas, effective stress is controlled during the pre-processing. The DEM code must include a robust servo-algorithm that can maintain the target stresses for these different control types while adjusting to abrupt changes in loading during a fitful sequence of seismic motion. This requirement was another challenging aspect of the simulations. The solution, part of the author's code, uses an adaptive control algorithm that maintains close fidelity to the target stresses and strains (see appendix in [45]).

Soil stiffness and, hence, seismic wave speed depend upon the mean effective stress (inter-granular stress): stiffness increases with depth, causing seismic waves to slow as they approach the ground surface. In physical modeling, this stress-dependence is the primary reason for using a centrifuge, rather than simply testing a scaled model at 1 g. A simple linear contact model in DEM yields no such pressure-dependence of the wave speed. A sphere-sphere Hertzian model also underestimates the dependence [1]; whereas, a cone-cone Hertzian model overestimates the dependence [27, 46]. For sands, the relationship between shear modulus G and mean effective stress, $\bar{p} = \frac{1}{3}\sigma'_{kk}$, is of the form $G \propto \bar{p}^\beta$, where the exponent β is typically near 0.50. DEM simulations with linear, sphere-sphere Hertzian, and cone-cone Hertzian contacts produce β values of 0, 0.42, and 0.56, respectively [46]. The author used a contact model of blunted cones, which gives an exponent of 0.50, mimicking that of Nevada Sand [46, 45].

The DEM contact model must also find tangential force. The two most common tangential models — the linear model and the Modified Mindlin (MM) model with a sphere-sphere Hertzian normal force — are inadequate for realistic simulations. The previous paragraph addressed the issue of pressure-dependence of a Hertzian sphere-sphere contact model. The MM model, however, suffers from another

deficiency, one that is particularly unsuitable for cyclic loading. In the MM model, the normal force is Hertzian; the incremental tangential stiffness is a monotonic increasing function of the normal force; and frictional slip occurs only when the tangential force equals the normal force times the friction coefficient [17,50]. Although easily implemented, the model is energetically inconsistent when the tangential force is below the friction limit, where deformation is assumed elastic. Unfortunately, a closed loading path that lies below the friction limit in the normal–tangential force-space can produce a spurious creation or loss of elastic energy. That is, with the MM model, energy is non-conservative for contact movements below the friction limit. This deficiency should be disallowed when modeling cyclic loading, since contacts will follow cyclic and unusual loading–unloading paths and must not produce energetically infeasible outcomes. The problem with the MM model is that it neglects the annular frictional slip that occurs within the contact zone between two particles, even when the tangential force has not yet reached the frictional limit. The phenomenon of annular slip was addressed by Mindlin [55] and Mindlin and Deresiewicz [46], but it is ignored in MM models. The paper uses an implementation of the full Mindlin and Deresiewicz solution, developed by Jaeger [33,41], and the model correctly accounts for annular slip and disallows energy creation.

3.6 Parallel processing

The model’s greatest computational demand is in the DEM calculations that are embedded within the dynamic and consolidation algorithms (line 10 in Fig. 4, and line 6 in Fig. 5). When reaching these steps, the N DEM assemblies are deformed in different amounts and directions, with each assembly loaded in a series of internal DEM time-steps. For these computations, the DEM assemblies can be assigned to different processing threads, and when all threads are complete, the algorithm returns to a single thread until the DEM assemblies are loaded again in the next Δt episode. The data of all DEM assemblies (contact forces, particle positions, etc.) are stored in shared memory, with a shared memory protocol (SMP). The OpenMP library was used in the paper’s simulations. Although not attempted in the current simulations, further speed-up could be attained with GPU parallelization of the RVE calculations (see [81]).

4 Examples

Four sets of documented centrifuge tests were simulated:

1. 11 m and 22 m level deposits of dense dry sand at $D_r = 100\%$ subjected to horizontal shaking with three seismic motions [69];
2. 10 m and 14 m level deposits of saturated sand at $D_r = 100\%$ subjected to horizontal shaking with three seismic motions [70,22];
3. 6 m level deposit of medium dense saturated sand at $D_r = 40\%$ that partially liquefies during horizontal seismic shaking [37]; and
4. 10 m deposit of medium-dense saturated sand at $D_r = 45\%$, 65% , and 75% , with a 5° slope that liquefies during dip-parallel near-sinusoid shaking [65,64].

The four centrifuge sets are summarized in Table 1.

Centrifuge tests are conducted at elevated accelerations on small models, which are intended to represent larger prototype systems. Scaling factors are applied to results of the model system to compute the corresponding prototype response [11]. Similar to centrifuge tests, the simulations herein were conducted at model-scale, avoiding the problem of matching the scales of multiple quantities in the prototype system (particle size, viscosity, stress, depth, surface tension, permeability, etc.). The simulation results were then converted to prototype-scale as with the centrifuge studies, so that results could be compared (acceleration response spectra, pore pressures, movements, etc.).

The sand in all tests was Nevada Sand, a fine uniformly graded sand (SP) used in many laboratory and centrifuge programs, including the VELACS program of the 1990s [4, 3,47]. For the centrifuge studies, sand was prepared as a homogeneous mass within a centrifuge box, and seismic base motions were applied in a single lateral direction with no intentional vertical motion. The containers were either flexible shear-beam or laminar ring type, creating nearly 1-D conditions in lateral directions (however, friction along side walls restricts vertical movement).

A series of DEM assemblies, each with 10,648 particles, was prepared to simulate Nevada Sand at a range of densities. Unlike FEM simulations in which a macro-scale constitutive model is chosen along with its macro-scale parameters, DEM simulations rely solely on micro-scale information. This information is of four types, listed in the order in which they are assigned: (1) a geometric description of the particles’ sizes and shapes and of their arrangement, (2) a contact normal-force model that defines the particles’ one-to-one displacement–force interactions, (3) a frictional contact model, and (4) a poromechanic relationship between pore volume and fluid pressure. Ideally, the macro-scale behavior of a DEM assembly resembles that of the intended soil, in regard to density, stiffness, and liquefaction resistance. The author relied upon laboratory tests of Nevada Sand conducted by Arulmoli [4] and Kwan [48] to check and calibrate the DEM assemblies’ properties.

DEM particles were created with a distribution of sizes similar to that of Nevada Sand, with a median size (by cumulative weight) $D_{50} = 0.165$ mm and a polydispersity $C_u = 2.1$. A non-spherical particle shape was adopted, be-

Table 1 Centrifuge tests: model characteristics.

Data Set	Soil D_{50} G_s	Prototype height H	Density D_r e	Saturation S_o	Slope α	Fluid viscosity μ
1) Stevens et al. [69]	N. S. #100 0.14 mm 2.67	11 m or 22 m	100% 0.563	0%	0°	$\mu_a = 0.019 \text{ mPa}\cdot\text{s}$
2) Stevens et al. [70,22,56]	N. S. #100 0.14 mm 2.67	10 m or 14 m	100% 0.563	100%	0°	$\mu_w = 8 \text{ mPa}\cdot\text{s}$
3) Sideras, Kramer [37,67]	N. S. #120 0.15 mm 2.68	6 m	40% 0.689	100%	0°	$\mu_w = 1 \text{ mPa}\cdot\text{s}$
4) Sharp et al. [63,65,64]	N. S. #120 0.15 mm 2.68	10 m	45%, 65%, 75% 0.605–0.718	100%	5°	$\mu_w = 50 \text{ mPa}\cdot\text{s}$

cause assemblies of spheres have less bulk strength than those of sands, and because the range of packing densities for spheres differs from that of sand particles. Although progress has been made to mimic the shapes of sand particles in DEM simulations [49], the author chose a simpler proxy shape: a non-convex cluster of seven overlapping spheres (see [46] for a rendering), allowing multiple contacts (interlocking) between two particles, and thus inhibiting inter-particle rolling. The correlations of Cho et al. [14] guided the selection of the relative sizes and overlaps of the seven spheres, leading to a particle shape that could be compacted to a range of void ratios similar to Nevada Sand. A suite of DEM assemblies was created, with void ratios ranging from 0.511 to 0.892 (see [45] for assembly protocol), similar to the range e_{\min} to e_{\max} of Arulmoli [4] (0.511 to 0.887). Different density ranges are reported in the various centrifuge studies, so the D_r value of each study was converted to a void ratio, and the DEM assembly with the closest void ratio was used for the study's simulation. At the start of each simulation, the assemblies were anisotropically consolidated (with zero lateral strain) to the geostatic conditions of the RVE points.

As described in Section 3.5, the contacts between particles were modeled as blunted cone asperities (see [41,46,44] for details). With this contact model, the shear modulus G was 104 MPa at mean stress $\bar{p} = 80 \text{ kPa}$ for strain γ of 0.0002% at void ratio $e = 0.653$, results similar to Arulmoli's tests on specimens with relative density $D_r = 60\%$. The contact profile produced a dependence of G on the mean stress \bar{p} , with proportionality $G \propto \bar{p}^{0.50}$, along with a dependence of G on e similar to Nevada Sand.

A DEM assembly's susceptibility to liquefaction is sensitive to the friction coefficient μ that is assigned to the particles' contacts. A coefficient of 0.40 was found to give results similar to the cyclic simple-shear tests of Kwan [48], noting that this type of testing is most similar to that of the centrifuge tests (i.e., vertical propagation of s-waves). The annular-slip contact model, described in Section 3.5, was

Table 2 Poromechanic parameters for DEM simulations (see [45]).

Property	Value
K_s , bulk modulus, grains	31.8 GPa
K_w , bulk modulus, liquid water	2.2 GPa
ν_s , Poisson ratio, grains	0.15
k_G , hydraulic conductivity	varies
μ_a , viscosity, air	0.019 mPa·s
μ_w , viscosity, water	varies
$p_{w,vap}$, vapor pressure, water	2.34 kPa
γ , surface tension, water–air	0.073 N/m
H^{cc} , Henry's solubility, water–air	0.0173
H^{cc} , Henry's solubility, water–CO ₂	0.878
p_{atm} , atmospheric pressure	100 kPa
D , bubble diameter	0.0001 m
S_o , initial saturation	Table 1

used to compute tangential forces that result from complex sequences of normal and tangential movements [41].

The poromechanic properties of the DEM assemblies are given in Table 2, and except for D , k_G and S_o , are accepted values for quartz, water, air, and CO₂. The assumed bubble diameter D is roughly the size of inter-grain pores, and its value is used to compute the dissolution of air in water for quasi-saturated mixtures. Although different hydraulic conductivities k_G have been reported for Nevada Sand, the simulation values were based on the results of Arulmoli [4], approximated as $k_G = (0.3 \text{ mm/s}) e^3 / (1 + e)$. The prototype permeability k of pore water varied among the tests, since viscosity additives were used to compensate, either wholly or partially, for acceleration scaling (see μ in Table 1).

The input base motions were obtained from published seismic acceleration records or were digitized from a study's figures. The simulations require the base displacements, so accelerations were double-integrated and, when necessary, adjusted to end with zero velocity.

4.1 Centrifuge Set 1

The first set of centrifuge tests was performed at the University of California, Davis, on a homogeneous, level, and dry deposit of dense sand with $D_r = 100\%$ [69]. The tests were performed on a model of 558 mm depth. Two tests were at a lower centrifuge speed (acceleration 20 g, DKS02_bb and DKS02_be), simulating an 11 m thick deposit; the third test, at a higher speed (acceleration 40 g, DKS02_bl), simulated a 22 m thickness. The centrifuge box was a flexible shear beam, and in the simulations, the sand's mass was increased by 24% to account for the box mass (e.g., [22]). Three seismic motions, taken from the same flight DKS02, were selected for simulation. The base motions were scaled versions of the 1989 Loma Prieta SCZ090 record, available from the Strong-Motion Virtual Data Center [12]. As was done in [22], the motions at model depth 483 mm (accelerometer A17) were used as input for the simulations. The data streams from all instruments are available from [56], and the full program is documented by Stevens et al. [69].

Figure 6 compares the acceleration response spectra near the ground surface for three base motions of the centrifuge and simulation tests. The spectra of the input base motions are also shown, and the figures are arranged with decreasing motion intensity from top to bottom. With the exception of the single test DKS02_be at periods less than 0.1 s, the simulations closely match the centrifuge results. For two of the tests, the simulations and centrifuge results are close across the full range of periods; for test DKS02_be, the match is close for periods above 0.1 s.

The sand is dense and dry, so one would expect dilation when vibrated at large strains. (Because lengths are reduced by a factor of 20, the air has an effective viscosity at prototype-scale that is 20 times less than that of air, thus making volume-change even more readily available.) Figure 7 shows the vertical accelerations at a prototype depth of about 2.5 m for the single motion DKS02_bb. Although the vertical accelerations are smaller than the input horizontal base accelerations (Fig. 7c), the two Figs. 7a and 7b show that the vertical accelerations were large (about 0.2 g) in both the centrifuge test and the simulation, with the largest vertical accelerations occurring at or shortly after the strongest base accelerations. Because the simulation's input base motion was purely horizontal, the vertical motions could only have been induced by a coupling of shear and vertical strains. Vertical movements are less regular in the centrifuge test (Fig. 7a), possibly because of vertical friction along the sides of the box, which would restrict and reflect movements within the model.

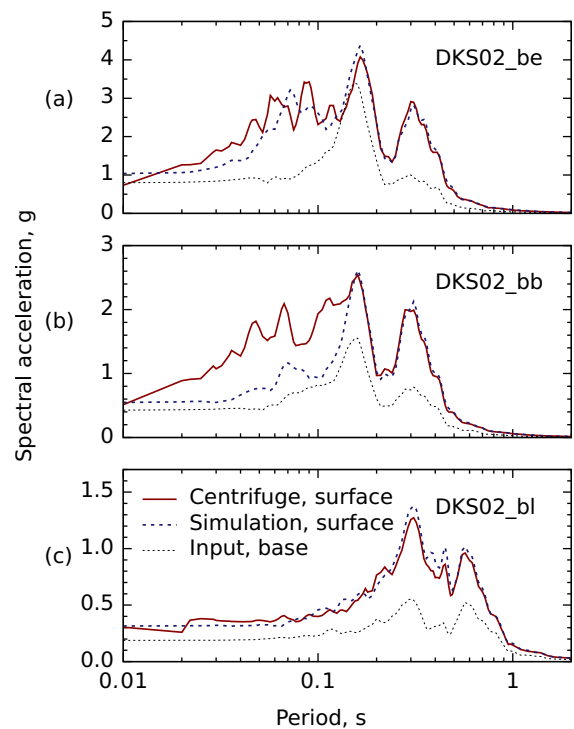


Fig. 6 Comparison of Set 1 acceleration response spectra for three base motions. The figures are arranged from top to bottom with decreasing peak base accelerations: (a) 0.79g, (b) 0.42g, and (c) 0.19g.

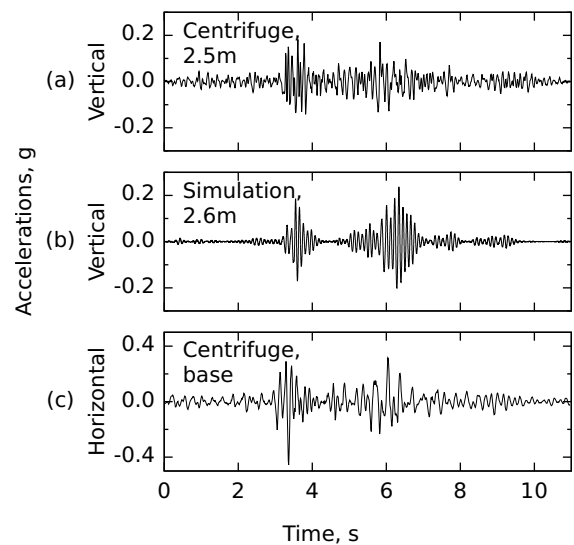


Fig. 7 Accelerations of Set 2 for test DKS02_bb (see Fig. 6b): (a) vertical accelerations for centrifuge test, depth 2.5 m, (b) vertical accelerations for the simulation, depth 2.6 m, and (c) horizontal base accelerations.

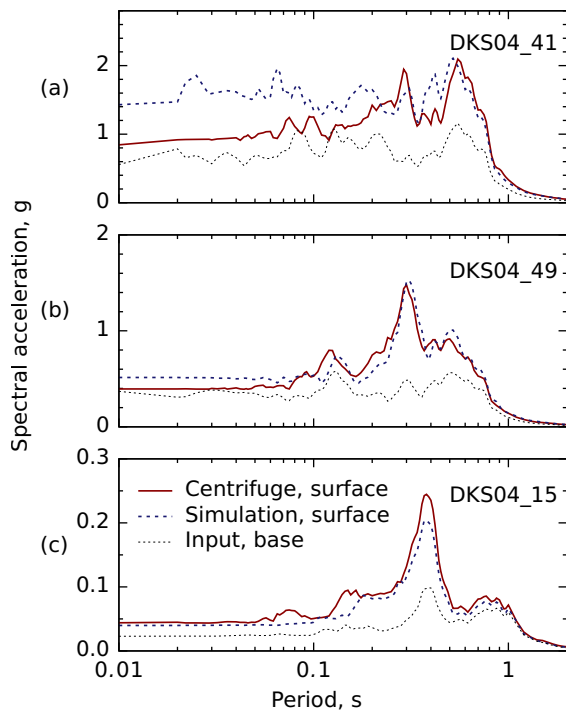


Fig. 8 Comparison of Set 2 horizontal acceleration response spectra for three base motions. The figures are arranged from top to bottom with decreasing peak base accelerations: (a) 0.50 g, (b) 0.25 g, and (c) 0.020 g.

4.2 Centrifuge Set 2

These tests were similar to those of Set 1, but the sand was saturated rather than dry. The model was a 553 mm deposit that was homogeneous and level, with $D_r = 100\%$ [70,22]. Two tests were conducted at a lower centrifuge speed (acceleration 18.1 g, DKS04.41 and DKS04.49), simulating a 10 m deposit; the third test, at a higher speed (acceleration 25.3 g, DKS04.15), simulated a 14 m deposit. Three base motions, taken from the single flight of experiment DKS04, were scaled versions of the SCZ090 record, available from the Strong-Motion Virtual Data Center [12]. (The same three motions were used in [22] to evaluate a continuum model of wave propagation.) As with Set 1, the sand mass was increased by 24% to account for the box mass. The base motions at model depth 471 mm (accelerometer A17) were used as input for the simulations [22]. The sand was saturated with a CO_2 protocol to remove air, whether in bubble or in dissolved form, and the absence of bubbles was verified with measurements of p-wave velocity. The data streams from all instruments are available from [56], and the full program is documented by Stevens et al. [70].

Surface acceleration response spectra are shown in Fig. 8 for centrifuge and simulation results of three motions, arranged from 8a to 8c with decreasing intensities (maximum prototype base accelerations of 0.50 g, 0.25 g, and 0.020 g). The simulations were run with the pore water

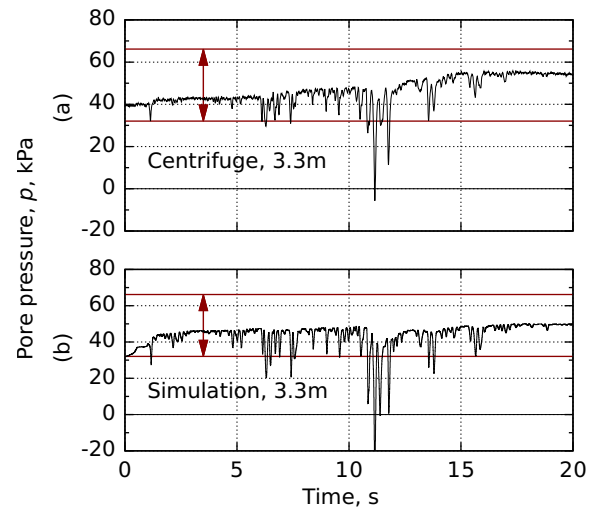


Fig. 9 Comparison of Set 2 water pressures for test DKS04.41 at prototype depth 3.3 m (see Fig. 8a): (a) centrifuge test, and (b) simulation. Arrows show the range between initial pressure and the full geostatic stress (r_u of 0 and 1, respectively).

devoid of gas, with no dissolved gas and no bubbles. The simulation results are close to those of the centrifuge tests at all periods for the mildest shaking of 8c; results are close for periods greater than 0.07 g for the modest shaking of Fig. 8b; and results are close for periods greater than 0.2 g for the most intense shaking of Fig. 8a.

To explore a possible reason for the poor spectrum results at short periods in the tests with the most intense shaking, water pressures are plotted at a depth of 3.3 m in Fig. 9 (pressures are relative to atmospheric pressure). In both the centrifuge test and the simulation, a general rise in water pressure is punctuated by abrupt drops, indicating strong but momentary dilation tendencies. These drops occur near peaks in the base acceleration. The larger simulation spectral response at short periods (Fig. 8a) is attributed to the large base accelerations between 10 s and 12 s. Notably, the largest drop, near 11 s, is much greater in the simulation than that measured with centrifuge instruments. Although the simulation in Figs. 8a and 9 was based on zero gas (air or CO_2) within the fluid, the author speculates that the pore water may have contained dissolved air, since test DKS04.41 occurred a week after the model was constructed and after multiple previous flights, providing time and opportunity for air to diffuse into the pore fluid. To investigate this possibility and the effect on accelerations, a second simulation was run with the pore water fully saturated with dissolved air at atmospheric pressure, but with no bubbles. Figure 10 compares the response spectrum of the second simulation with the centrifuge results. The simulation spectrum with dissolved air is closer to the centrifuge results than the simulation with no gas, although the new simulation does over-estimate accelerations for short periods. This example suggests the possibility of bubble

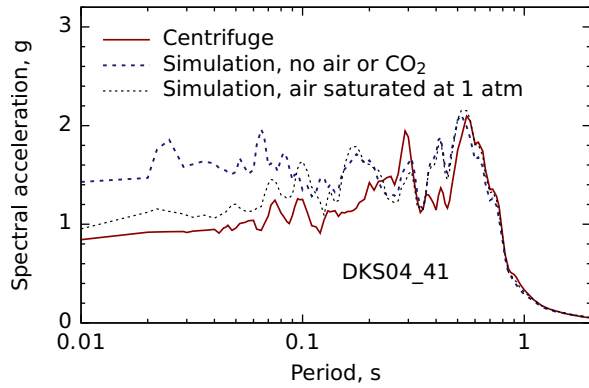


Fig. 10 Comparison of Set 2 acceleration response spectra for test DKS04_41. Two simulations are shown: one with all gas removed, and one with the pore fluid saturated with dissolved air.

cavitation during dilation and illustrates the importance of pore-fluid characteristics in wave propagation.

4.3 Centrifuge Set 3

Set 3 was conducted at Rensselaer Polytechnic Institute on a saturated homogeneous level deposit of medium dense sand at $D_r = 40\%$ [37,67]. The 267 mm deep sand was underlaid with a layer of cemented sand, and the input base motions were those recorded at the top of this cemented material. The centrifuge acceleration of 22.5 g produced a prototype depth of 6 m. Unlike Sets 1 and 2, the box was a laminar ring type, and the mass of the rings, which are separated by low-friction rollers, must be included with the sand mass, by applying a factor of 1.294 to the soil density ρ in Eqs. (1), (9)–(13), and (25)–(26) (see [72] for full explanation of the factor). Although the original program included several flights with multiple shaking events, the simulation was of a single motion that is described in [67] (Experiment 3, Test 3), using centrifuge data that is available in [37]. The sand was saturated with a CO_2 protocol.

The centrifuge study investigated liquefaction and pore pressure build-up during seismic motion, with pore water pressures, accelerations, and settlements measured at six depths. Figure 11 shows pore pressures that were recorded at three depths during the brief shaking event. Results are expressed as the excess pore pressure ratio r_u , equal to pressure above the hydrostatic condition divided by the difference between the geostatic and hydrostatic stresses. The ratio lies between 0 and 1, with 1 representing full liquefaction (larger values were computed for the shallowest instrument, probably due to the assumed instrument depth). Both the centrifuge and simulation results show a rise in pore pressure during shaking, with the greatest ratios attained at shallower depths. At 0.5 m, abrupt downward drops in pressure (indicating a dilation tendency) coincided

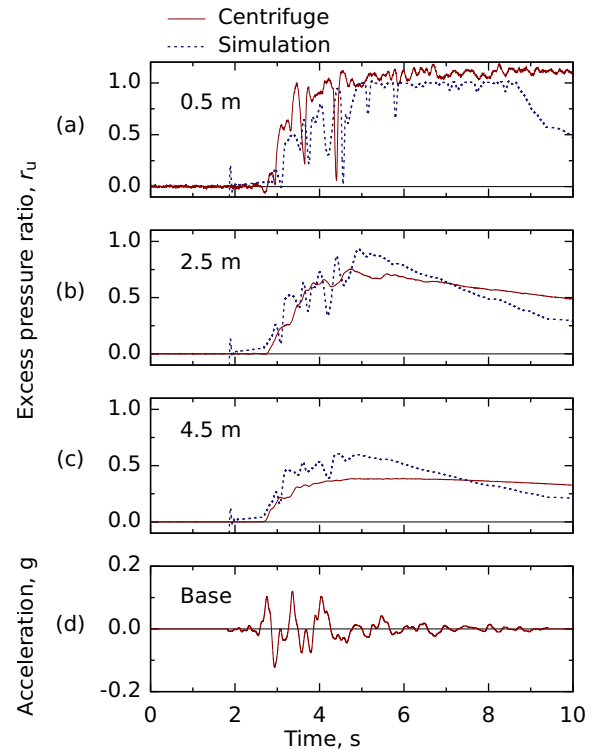


Fig. 11 Comparison of Set 3 pore pressure ratios: (a)–(c) ratios at three depths, and (d) horizontal base acceleration.

for the experiment and simulation, and the sand liquefied at about 5 s.

As shaking wanes, water pressures are seen to decrease due to concurrent consolidation (Fig. 11). Although the simulation predicts the rise in water pressure, it gives a more rapid drop-off in pressure when shaking subsides. Measured centrifuge pressures returned to the hydrostatic condition at about 60 s; whereas, this condition occurred at 20 s in the simulation. In geotechnical practice, the rate of consolidation is quantified with the consolidation coefficient, c_v (akin to a diffusion coefficient), which is proportional to both the permeability and the constrained uniaxial stiffness of the grain matrix. The more rapid consolidation of the simulation is due to its greater post-shaking stiffness, which is confirmed by the simulation's smaller eventual settlement: the final settlement in the centrifuge model was 3 cm; whereas, the final settlement of the simulation was 0.8 cm.

4.4 Centrifuge Set 4

The fourth set was conducted at Rensselaer Polytechnic Institute on a sloping 10 m deep (prototype) homogeneous deposit of saturated sand with densities D_r of 45%, 65%, and 75%. [63,65,64]. To study lateral spreading, the model was configured to simulate a 5° slope that was submerged beneath a level water surface [72]. The centrifuge model

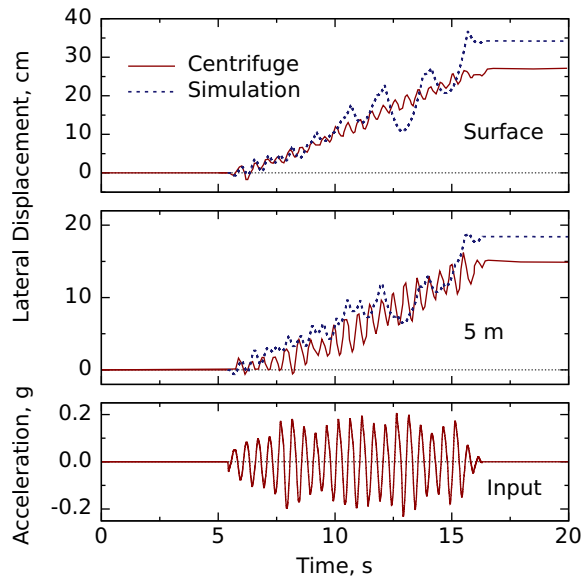


Fig. 12 Comparison of Set 4 lateral down-slope displacements for test L65V-2-10 ($D_r = 65\%$) at the surface and at depth 5 m. Base input accelerations are shown in the lower panel.

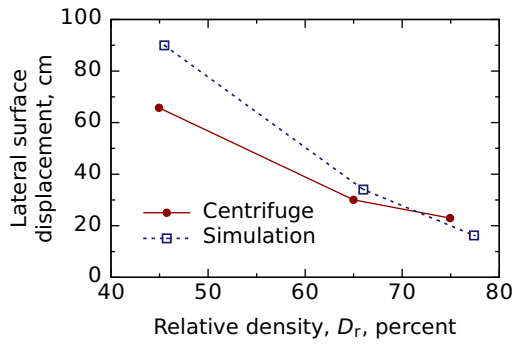


Fig. 13 Comparison of Set 4 lateral down-slope surface displacements for three densities.

was 20 cm deep and spun at 50 g. As with Set 3, soil density was multiplied by 1.294 to account for the laminar rings. The sand was saturated with a vacuum protocol, and the simulations were run by assuming the pore water was devoid of gas, whether dissolved and in bubbles. The water was treated with additives to produce a viscosity 50 times greater than that of pure water.

The base motion was a near-sinusoid application of 22 cycles of acceleration amplitude ≈ 0.20 g at 2 Hz, with a peak acceleration of 0.23 g. The acceleration record and centrifuge results were digitized from plots of Sharp [63].

Figure 12 shows down-slope lateral movements at two depths during shaking of the model with $D_r = 65\%$. The simulation tracks the centrifuge results until the final few cycles of acceleration, when the simulation ends with about 25% more lateral movement than the centrifuge model. Figure 13 shows the final lateral displacements of tests with three densities. The simulations give similar movements as

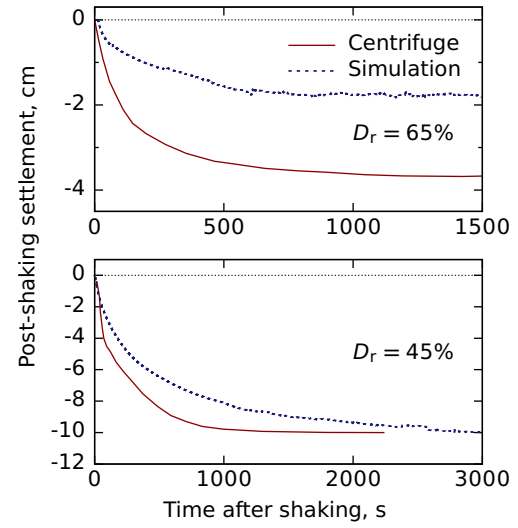


Fig. 14 Comparison of Set 4 post-shaking surface settlements for tests L65V-2-10 and L45V-2-10 (densities $D_r = 65\%$ and 45%).

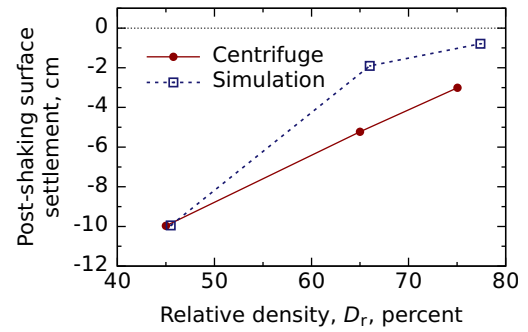


Fig. 15 Comparison of Set 4 surface settlements for three densities.

in the centrifuge models, with decreasing lateral movement as density is increased.

Surface settlements are compared in Fig. 14 for two densities: $D_r = 45\%$ and 65% . Only post-shaking settlements are shown, because of what the author considers anomalous settlements during shaking in the centrifuge models. For both densities, the centrifuge models settled 3–7 cm in less than 5 s during the 10 s of shaking, with the larger settlement occurring in the denser model. These results could have been caused by local movements of the settlement pads, so shaking settlements are removed in the post-shaking consolidation results of Fig. 14. For the looser condition, the simulation closely agrees with the centrifuge results, but the simulation underestimates settlement in the denser test. Figure 15 shows the final settlements of tests with three densities. In both simulations and centrifuge tests, settlement decreases with density, although settlement is underestimated with the denser tests.

4.5 Hardware performance

The simulations were run on a 2-socket, 14 cores-per-socket, 2 threads-per-core Intel Xeon E5-2690 2.60GHz server (introduced in 2012). Each simulation was given 10 threads so that several simulations could be run concurrently. Each simulation required 6GB of RAM and between 12 and 40 hours to run. The simulations in Sections 4.1–4.4 were run with an N number of RVEs of 17, 17, 18, and 20, respectively, with each RVE being a DEM assembly of 10,648 sphere-cluster particles.

5 Conclusions

A multi-phase, multi-scale method is developed for modeling and predicting wave propagation and the weakening and liquefaction of near-surface soils. Verification results are promising: response spectra are close to those of centrifuge models; the rise and fluctuation of pore water pressure during shaking are similar to those of centrifuge models; down-slope lateral movements are predicted within a few tens percent; and surface settlement are roughly in accord with those of the physical models. The most notable variance is the stiffer post-shaking settlement response of the simulations, a difference that is most likely due to the simulations' use of sphere-cluster particles rather than more realistic grain shapes. The paper's simple examples were conducted as a verification exercise but are limited in their complexity, and most of the model's twenty possibilities that were listed in the Introduction are not explored herein but await further study. The results show that the method promises better understanding of the diverse phenomena that occur during ground shaking, and the method's results are sufficiently favorable to warrant use in predicting site response and liquefaction potential.

The model certainly has limitations, but it can also be extended to solve more general problems than those listed in the Introduction. Some modest extensions to the model would permit conditions such as the following: (1) investigating soil-structure interaction by modeling a single or multiple degree-of-freedom (SDOF or MDOF) building system atop the soil column; (2) extending the field equations to model multiple pore fluids that form continuous commingled fluid networks; and (3) augmenting the current rigid (reflecting) rock base with a compliant (absorbing) base, allowing deconvolution of surface motions.

The model is limited by its one-dimensional nature and by the computational demands of modeling large assemblies of particles. A one-dimensional model can not simulate the non-homogeneity across a site, which gives rise to sand boils and other localized phenomena [52, 13]. The examples have also taken advantage of the narrow size disparity of Nevada Sand particles, but DEM computation

time increases greatly with wider polydispersity, such that soils with a size range of more than an order of magnitude (e.g. silty sands and plastic soils) will increase runtimes by several times those of the paper's simulations.

A Poromechanics of dry soil

The poroelastic characteristics of dry soil are rarely considered in geomechanics, due to the wide difference in the stiffnesses of air and of the solid matrix. However, just as with water, the paper's algorithm requires the stiffnesses of all pore fluids, whether water, air, or quasi-saturated water. The air of a dry soil is assumed to obey the ideal gas law,

$$pV_v = \bar{N}RT \quad (38)$$

where \bar{N} is the gas substance (moles) of air in the void volume V_v ; T is the absolute temperature; and R is the ideal gas constant. Assuming that temperature is constant, the initial and current values of quantity pV_v/\bar{N} are equal, so that the current pressure is

$$p = p_o \frac{\bar{N}}{\bar{N}_o} \frac{V_{vo}}{V_v} \quad (39)$$

where p_o is the initial air pressure; V_v and V_{vo} are the current and initial void volumes; and \bar{N} and \bar{N}_o are the current and initial moles of air. The ratio \bar{N}/\bar{N}_o is equal to the ratio $\det(\mathbf{F})/\det(\mathbf{W})$, as described near the beginning of Section 3. Multiplying and dividing Eq. (39) by total soil volume V_o and noting that V_{vo}/V_o is the initial porosity n_o , we have

$$p = p_o n_o \frac{\det(\mathbf{F})}{\det(\mathbf{W})} \frac{V_o}{V_v} \quad (40)$$

The current void volume V_v is the difference of the total volume V and solid volume V_s ,

$$\begin{aligned} V_v &= V - V_s \\ &= V_o \left[\det(\mathbf{F}) - (1 - n_o) \left(1 + \frac{\sigma'_{kk} - \sigma'_{o,kk}}{3K_s} - \frac{p - p_o}{K_s} \right) \right] \end{aligned} \quad (41)$$

where K_s is the bulk modulus of the solid grains; $\det(\mathbf{F}) = V/V_o$ is the determinant (Jacobian) of the deformation gradient (i.e., the ratio of the current and initial soil volumes); and $1 - n_o = V_{so}/V_o$ is the initial solid fraction. This equation accounts for the combined changes in the volumes of the grains due to changes in the air pressure and in the contact forces, by assuming that the grains are composed of a linear-elastic material [8, 82, 45].

Substituting Eq. (41) into Eq. (40), we have the following quadratic equation for pressure p :

$$Ap^2 + Bp + C = 0 \quad (42)$$

$$A = (1 - n_o)/K_s \quad (43)$$

$$B = \det(\mathbf{F}) - (1 - n_o) \left[1 + (\sigma'_{kk} - \sigma'_{o,kk})/3K_s \right] \quad (44)$$

$$C = p_o n_o \det(\mathbf{F})/\det(\mathbf{W}) \quad (45)$$

and the following equation for fluid outflow $\det(\mathbf{W})$:

$$\begin{aligned} \det(\mathbf{W}) &= \frac{p_o n_o \det(\mathbf{F})}{p} \\ &\quad / \left[\det(\mathbf{F}) - (1 - n_o) \left(1 + \frac{\sigma'_{kk} - \sigma'_{o,kk}}{3K_s} - \frac{p - p_o}{K_s} \right) \right] \end{aligned} \quad (46)$$

In a one-dimensional setting, $\det(\mathbf{W}) = 1 + du_3/dX_3 + dw_3/dX_3$ and $\det(\mathbf{F}) = 1 + du_3/dX_3$, where w_3 is the pore fluid displacement relative to the matrix displacement u_3 , and the X_3 is the original position within the soil column.

Data availability: The simulations in this paper were performed with the program DEMPLA, “Discrete Element Method for Propagation and Liquefaction Analysis.” The program is available on GitHub in the repository <https://github.com/mrkuhn53/dempl>, which includes source code, documentation, and examples [42].

Acknowledgment: The high-performance computer described in Section 4.5 was a generous donation from The Donald P and Darlene V Shiley Trust to the Donald P. Shiley School of Engineering.

References

1. Agnolin, I., Roux, J.N.: Internal states of model isotropic granular packings. III. elastic properties. *Phys. Rev. E* **76**, 061304 (2007). DOI <https://doi.org/10.1103/PhysRevE.76.061304>
2. Al-Jibury, F.K.: Saturated water permeability of soils as related to air permeability at different moisture tension. Master, Oregon State University (1960)
3. Arulmoli, K.: VELACS: selection, distribution and laboratory testing of soils. In: K. Arulanandan, R.F. Scott (eds.) *Verifications of Numerical Procedures for the Analysis of Soil Liquefaction Problems*, vol. 2, pp. 1281–1292. Balkema, Rotterdam (1994)
4. Arulmoli, K., Muraleetharan, K.K., Hossain, M.M., Fruth, L.S.: VELACS verification of liquefaction analyses by centrifuge studies laboratory testing program soil data report. Tech. Rep. Project No. 90-0562, The Earth Technology Corporation, Irvine, CA (1992). Data available through <http://yees.usc.edu/velacs>
5. Bagi, K.: Stress and strain in granular assemblies. *Mech. of Mater.* **22**(3), 165–177 (1996). DOI [https://doi.org/10.1016/0167-6636\(95\)00044-5](https://doi.org/10.1016/0167-6636(95)00044-5)
6. Bardet, J.P.: Numerical simulations of the incremental responses of idealized granular materials. *Int. J. Solids Struct.* **10**(8), 879–908 (1994). DOI [https://doi.org/10.1016/0749-6419\(94\)90019-1](https://doi.org/10.1016/0749-6419(94)90019-1)
7. Biot, M.A.: Mechanics of deformation and acoustic propagation in porous media. *J. Appl. Physics* **33**(4), 1482–1498 (1962). DOI <https://doi.org/10.1063/1.1728759>
8. Biot, M.A., Willis, D.G.: The elastic coefficients of the theory of consolidation. *J. Appl. Mech.* **15**, 594–601 (1957)
9. Bouckovalas, G.D., Tsiapas, Y.Z., Zontanou, V.A., Kalogeraki, C.G.: Equivalent linear computation of response spectra for liquefiable sites: the spectral envelope method. *J. Geotech. and Geoenv. Eng.* **143**(4), 04016115 (2017). DOI [https://doi.org/10.1061/\(ASCE\)GT.1943-5606.0001625](https://doi.org/10.1061/(ASCE)GT.1943-5606.0001625)
10. Bray, J.D., Boulanger, R.W., Cubrinovski, M., Tokimatsu, K., Kramer, S.L., O'Rourke, T., Rathje, E., Green, R.A., Robertson P. K. and Beyzaei, C.Z.: Liquefaction-induced ground movement effects: U.S.–new zealand-japan international workshop. PEER Repor 2017/02, Pacific Earthquake Engineering Research Center, University of California, Berkeley (2017)
11. Butterfield, R.: Scale-modelling of fluid flow in geotechnical centrifuges. *Soils and Found.* **40**(6), 39–45 (2000). DOI <https://doi.org/10.3208/sandf.40.6.39>
12. Center for Engineering Strong Motion Data: Strong-Motion Virtual Data Center (VDC) (2021). URL <https://www.strongmotioncenter.org/vdc/scripts/default.plx>
13. Chakraborty, P., Popescu, R.: Numerical simulation of centrifuge tests on homogeneous and heterogeneous soil models. *Comput. and Geotech.* **41**, 95–105 (2012). DOI <https://doi.org/10.1016/j.compgeo.2011.11.008>
14. Cho, G.C., Dodds, J., Santamarina, J.C.: Particle shape effects on packing density, stiffness, and strength: natural and crushed sands. *J. Geotech. and Geoenv. Eng.* **132**(5), 591–602 (2006). DOI [https://doi.org/10.1061/\(ASCE\)1090-0241\(2007\)133:1\(1474\)](https://doi.org/10.1061/(ASCE)1090-0241(2007)133:1(1474))
15. Cleary, P.W., Sinnott, M., Morrison, R.: Prediction of slurry transport in SAG mills using SPH fluid flow in a dynamic dem based porous media. *Minerals Engineering* **19**(15), 1517–1527 (2006). DOI <https://doi.org/10.1016/j.mineng.2006.08.018>
16. da Cruz, F., Emam, S., Prochnow, M., Roux, J.N., Chevoir, F.: Rheophysics of dense granular materials: Discrete simulation of plane shear flows. *Phys. Rev. E* **72**(2), 021309 (2005). DOI <https://doi.org/10.1103/PhysRevE.72.021309>
17. Cundall, P.A.: Computer simulations of dense sphere assemblies. In: M. Satake, J. Jenkins (eds.) *Micromechanics of Granular Materials*, pp. 113–123. Elsevier Science Pub. B.V., Amsterdam, The Netherlands (1988)
18. Deierlein, G.G., Zsárczay, A.: State of the art in computational simulation for natural hazards engineering. Report 2021-01, NHERI Center for Computational Modeling and Simulation, 2nd Edition (2021). DOI [DOI:10.5281/zenodo.2579581](https://doi.org/10.5281/zenodo.2579581)
19. El Shamy, U., Abdelhamid, Y.: Modeling granular soils liquefaction using coupled lattice Boltzmann method and discrete element method. *Soil Dyn. Earthq. Eng.* **67**, 119–132 (2014). DOI <https://doi.org/10.1016/j.soildyn.2014.09.004>
20. El Shamy, U., Zeghal, M.: Coupled continuum-discrete model for saturated granular soils. *J. Eng. Mech.* **131**(4), 413–426 (2005). DOI [https://doi.org/10.1061/\(ASCE\)0733-9399\(2005\)131:4\(413\)](https://doi.org/10.1061/(ASCE)0733-9399(2005)131:4(413))
21. El Shamy, U., Zeghal, M.: A micro-mechanical investigation of the dynamic response and liquefaction of saturated granular soils. *Soil Dyn. Earthq. Eng.* **27**(8), 712–729 (2007). DOI <https://doi.org/10.1016/j.soildyn.2006.12.010>
22. Elgamal, A., Yang, Z., Lai, T., Kutter, B.L., Wilson, D.W.: Dynamic response of saturated dense sand in laminated centrifuge container. *J. Geotech. and Geoenv. Eng.* **131**(5), 598–609 (2005). DOI [https://doi.org/10.1061/\(ASCE\)1090-0241\(2005\)131:5\(598\)](https://doi.org/10.1061/(ASCE)1090-0241(2005)131:5(598))
23. Elgamal, A.W., Zeghal, M., Tang, H.T., Stepp, J.C.: Logging downhole array. I: Evaluation of site dynamic properties. *J. Geotech. Eng.* **121**(4), 350–362 (1995). DOI [https://doi.org/10.1061/\(ASCE\)0733-9410\(1995\)121:4\(350\)](https://doi.org/10.1061/(ASCE)0733-9410(1995)121:4(350))
24. Faybishenko, B.A.: Hydraulic behavior of quasi-saturated soils in the presence of entrapped air: Laboratory experiments. *Water Resour. Res.* **31**(10), 2421–2435 (1995). DOI <https://doi.org/10.1029/95WR01654>
25. Fredlund, D.G.: Density and compressibility characteristics of air–water mixtures. *Can. Geotech. J.* **13**(4), 386–396 (1976). DOI <https://doi.org/10.1139/t76-040>
26. Fredlund, D.G.: Unsaturated soil mechanics in engineering practice. *J. Geotech. and Geoenv. Eng.* **132**(3), 286–321 (2006). DOI [https://doi.org/10.1061/\(ASCE\)1090-0241\(2006\)132:3\(286\)](https://doi.org/10.1061/(ASCE)1090-0241(2006)132:3(286))
27. Goddard, J.D.: Nonlinear elasticity and pressure-dependent wave speeds in granular media. *Proc. R. Soc. Lond. A* **430**, 105–131 (1990). DOI <https://doi.org/10.1098/rspa.1990.0083>
28. Goodarzi, M., Kwok, C.Y., Tham, L.G.: A continuum-discrete model using Darcy's law: formulation and verification. *Int. J. Numer. and Anal. Methods in Geomech.* **39**(3), 327–342 (2015). DOI <https://doi.org/10.1002/nag.2319>
29. Guo, N., Zhao, J.: A coupled FEM/DEM approach for hierarchical multiscale modelling of granular media. *Int. J. Numer. Methods Eng.* **99**(11), 789–818 (2014). DOI <https://doi.org/10.1002/nme.4702>
30. Hashash, Y.M.A., Dashti, S., Romero, M.I., Ghayoomi, M., Musgrove, M.: Evaluation of 1-D seismic site response modeling of sand using centrifuge experiments. *Soil Dyn. Earthq. Eng.* **78**, 19–31 (2015). DOI <https://doi.org/10.1016/j.soildyn.2015.07.003>
31. Holzer, T.L., Hanks, T.C., Youd, T.L.: Dynamics of liquefaction during the 1987 Superstition Hills, California,

- earthquake. *Science* **244**(4900), 56–59 (1989). DOI [DOI:10.1126/science.244.4900.56](https://doi.org/10.1126/science.244.4900.56)
32. Idriss, I.M., Boulanger, R.W.: Semi-empirical procedures for evaluating liquefaction potential during earthquakes. *Soil Dynamics and Earthquake Engineering* **26**(2), 115–130 (2006). DOI <https://doi.org/10.1016/j.soildyn.2004.11.023>
 33. Jäger, J.: *New Solutions in Contact Mechanics*. WIT Press, Southampton, UK (2005)
 34. Jop, P., Forterre, Y., Pouliquen, O.: A constitutive law for dense granular flows. *Nature* **441**(7094), 727–730 (2006)
 35. Kloss, C., Goniva, C., Hager, A., Amberger, S., Pirker, S.: Models, algorithms and validation for opensource dem and cfd-dem. *Progress in Computational Fluid Dynamics* **12**(2/3), 140–152 (2012)
 36. Kokusho, T.: Correlation of pore-pressure B-value with P-wave velocity and poisson's ratio for imperfectly saturated sand or gravel. *Soils and Found.* **40**(4), 95–102 (2000). DOI <https://doi.org/10.3208/sandf.40.4.95>
 37. Kramer, S.: Evolutionary intensity measures for more accurate and informative liquefaction hazard evaluation. Tech. Rep. NEES-2010-0957, NHERI Design-Safe Data Depot (2010). URL <https://www.designsafe-ci.org/data/browser/public/nees.public/NEES-2010-0957.groups>
 38. Kramer, S.L., Sideras, S.S., Greenfield, M.W.: The timing of liquefaction and its utility in liquefaction hazard evaluation. *Soil Dyn. Earthq. Eng.* **91**, 133–146 (2016)
 39. Ku, T., Subramanian, S., Moon, S.W., Jung, J.: Stress dependency of shear-wave velocity measurements in soils. *J. Geotech. and Geoenv. Eng.* **143**(2), 04016092 (2017)
 40. Kuhn, M.R.: Are granular materials simple? An experimental study of strain gradient effects and localization. *Mech. of Mater.* **37**(5), 607–627 (2005). DOI <https://doi.org/10.1016/j.mechmat.2004.05.001>
 41. Kuhn, M.R.: Implementation of the Jäger contact model for discrete element simulations. *Int. J. Numer. Methods Eng.* **88**(1), 66–82 (2011). DOI <https://doi.org/10.1002/nme.3166>
 42. Kuhn, M.R.: DEMPLA and OVAL: programs for analyzing particle assemblies and for simulating wave propagation and liquefaction with the discrete element method (2021). URL <https://github.com/mrkuhn53/dempla/tree/master/>
 43. Kuhn, M.R., Daouadji, A.: Multi-directional behavior of granular materials and its relation to incremental elastoplasticity. *Int. J. Solids Struct.* **152–153**, 305–323 (2018). DOI <https://doi.org/10.1016/j.ijsolstr.2018.07.005>
 44. Kuhn, M.R., Daouadji, A.: Quasi-static incremental behavior of granular materials: Elastic-plastic coupling and micro-scale dissipation. *J. Mech. Phys. Solids* **114**, 219–237 (2018). DOI <https://doi.org/10.1016/j.jmps.2018.02.019>
 45. Kuhn, M.R., Daouadji, A.: Simulation of undrained quasi-saturated soil with pore pressure measurements using a discrete element (DEM) algorithm. *Soils and Found.* **60**(5), 1097–1111 (2020). DOI <https://doi.org/10.1016/j.sandf.2020.05.013>
 46. Kuhn, M.R., Renken, H., Mixsell, A., Kramer, S.: Investigation of cyclic liquefaction with discrete element simulations. *J. Geotech. and Geoenv. Eng.* **140**(12), 04014075 (2014). DOI [https://doi.org/10.1061/\(ASCE\)GT.1943-5606.0001181](https://doi.org/10.1061/(ASCE)GT.1943-5606.0001181)
 47. Kutter, B.L., Chen, Y.R., Shen, C.K.: Triaxial and torsional shear test results for sand. Tech. Rep. CR 94.003, Office of Naval Research, Arlington, VA (1994)
 48. Kwan, W.S.: Laboratory investigation into evaluation of sand liquefaction under transient loadings. Dissertation, University of Texas at Austin (2015)
 49. Lim, K.W., Andrade, J.E.: Granular element method for three-dimensional discrete element calculations. *Int. J. Numer. and Anal. Methods in Geomech.* **38**(2), 167–188 (2014). DOI <https://doi.org/10.1016/j.cma.2012.06.012>
 50. Lin, X., Ng, T.T.: A three-dimensional discrete element model using arrays of ellipsoids. *Géotechnique* **47**(2), 319–329 (1997). DOI <https://doi.org/10.1680/geot.1997.47.2.319>
 51. Lloret, A., Alonso, E.E.: Consolidation of unsaturated soils including swelling and collapse behaviour. *Géotechnique* **30**(4), 449–477 (1980). DOI <https://doi.org/10.1680/geot.1980.30.4.449>
 52. Maharjan, M., Takahashi, A.: Centrifuge model tests on liquefaction-induced settlement and pore water migration in non-homogeneous soil deposits. *Soil Dyn. Earthq. Eng.* **55**, 161–169 (2013). DOI <https://doi.org/10.1016/j.soildyn.2013.09.002>
 53. Manzari, M.T., El Ghorab, M., Kutter, B.L., Zeghal, M., Abdoun, T., Arduino, P., Armstrong, R.J., Beaty, M., Carey, T., Chen, Y., et al.: Liquefaction experiment and analysis projects (LEAP): Summary of observations from the planning phase. *Soil Dyn. Earthq. Eng.* **113**, 714–743 (2018). DOI <https://doi.org/10.1016/j.soildyn.2017.05.015>
 54. McManus, K.J., Davis, R.O.: Dilation-induced pore fluid cavitation in sands. *Géotechnique* **47**(1), 173–177 (1997). DOI <https://doi.org/10.1680/geot.1997.47.1.173>
 55. Mindlin, R.D.: Compliance of elastic bodies in contact. *J. Appl. Mech.* **16**, 259–268 (1949)
 56. Center for Geotechnical Modeling: University of California, Davis (2021). URL <https://cgm.engr.ucdavis.edu/about/>
 57. Ng, T.T.: Input parameters of discrete element methods. *J. Eng. Mech.* **132**(7), 723–729 (2006). DOI [https://doi.org/10.1061/\(ASCE\)0733-9399\(2006\)132:7\(723\)](https://doi.org/10.1061/(ASCE)0733-9399(2006)132:7(723))
 58. Ordóñez, G.A.: SHAKE2000: A computer program for the 1D analysis of geotechnical earthquake engineering problems. Geomotions, LLC, USA, Lacey, WA, USA (2000)
 59. O'Sullivan, C., Bray, J.D.: Selecting a suitable time step for discrete element simulations that use the central difference time integration scheme. *Eng. Comput.* **21**(2/3/4), 278–303 (2004). DOI <https://doi.org/10.1108/02644400410519794>
 60. Otsubo, M., O'Sullivan, C., Hanley, K.J., Sim, W.W.: The influence of particle surface roughness on elastic stiffness and dynamic response. *Géotechnique* **67**(5), 452–459 (2017). DOI <https://doi.org/10.1680/jgeot.16.P.050>
 61. Rahman, M.M., Baki, M.A.L., Lo S, R.: Prediction of undrained monotonic and cyclic liquefaction behavior of sand with fines based on the equivalent granular state parameter. *Int. J. Geomech.* **14**(2), 254–266 (2014). DOI [https://doi.org/10.1061/\(ASCE\)GM.1943-5622.0000316](https://doi.org/10.1061/(ASCE)GM.1943-5622.0000316)
 62. Schnabel, P.B., Lysmer, J., Seed, H.B.: SHAKE: A computer program for earthquake response of horizontally layered sites. Tech. Rep. Report EERC-72/12, Earthquake Engineering Research Center, University of California Berkeley (1972)
 63. Sharp, M.K.: Development of centrifuge based prediction charts for liquefaction and lateral spreading from cone penetration testing. Ph.d. thesis, Rensselaer Polytechnic Institute, Trou, N.Y. (1999)
 64. Sharp, M.K., Dobry, R.: Sliding block analysis of lateral spreading based on centrifuge results. *Int. J. Phys. Model. Geotech.* **2**(2), 13–32 (2002). DOI <https://doi.org/10.1680/ijpmg.2002.020202>
 65. Sharp, M.K., Dobry, R., Abdoun, T.: Liquefaction centrifuge modeling of sands of different permeability. *J. Geotech. and Geoenv. Eng.* **129**(12), 1083–1091 (2003). DOI [https://doi.org/10.1061/\(ASCE\)1090-0241\(2003\)129:12\(1083\)](https://doi.org/10.1061/(ASCE)1090-0241(2003)129:12(1083))
 66. Shimizu, Y.: Fluid coupling in PFC2D and PFC3D. In: Y. Shimizu, R. Hart, P. Cundall (eds.) *Numerical Modeling in Micromechanics Via Particle Methods*. Proc. of the 2nd International PFC Symposium, Kyoto, Japan, pp. 281–287. AA Balkema Leiden, Netherlands (2004)
 67. Sideras, S.S.: Evolutionary intensity measures for more accurate and informative evaluation of liquefaction triggering. Dissertation, University of Washington, Seattle, Wash. (2019)
 68. Sitharam, T., Vinod, J.: Numerical simulation of liquefaction and pore pressure generation in granular materials using DEM. *Int. J. Geotech. Engrg.* **2**(2), 103–113 (2008)

69. Stevens, D.K., Kim, B.I., Wilson, D.W., Kutter, B.L.: Comprehensive investigation of nonlinear site response–centrifuge data report for DKS02. Tech. Rep. Data Report UCD/CGMDR-99/02, Center for Geotechnical Modeling, Univ. of Cal., Davis (1999)
70. Stevens, D.K., Kim, B.I., Wilson, D.W., Kutter, B.L.: Comprehensive investigation of nonlinear site response–centrifuge data report for DKS04. Tech. Rep. Data Report UCD/CGMDR-01/03, Center for Geotechnical Modeling, Univ. of Cal., Davis (2001)
71. Suzuki, K., Kuhn, M.R.: Uniqueness of discrete element simulations in monotonic biaxial shear tests. *Int. J. Geomech.* **14**(5), 06014010 (2014). DOI [https://doi.org/10.1061/\(ASCE\)GM.1943-5622.0000365](https://doi.org/10.1061/(ASCE)GM.1943-5622.0000365)
72. Taboada-Urtuzuástegui: Centrifuge modeling of earthquake-induced lateral spreading in sand using a laminar box. Ph.d. thesis, Rensselaer Polytechnic Institute, Troy, N.Y. (1995)
73. Taboada-Urtuzuástegui, V.M., Dobry, R.: Centrifuge modeling of earthquake-induced lateral spreading in sand. *J. Geotech. and Geoenv. Eng.* **124**(12), 1195–1206 (1998). DOI [https://doi.org/10.1061/\(ASCE\)1090-0241\(1998\)124:12\(1195\)](https://doi.org/10.1061/(ASCE)1090-0241(1998)124:12(1195))
74. Terzaghi, K.: *Theoretical Soil Mechanics*. J. Wiley and Sons, New York (1943)
75. Thevanayagam, S., Kanagalingam, T., Reinhorn, A., Tharmendhira, R., Dobry, R., Pitman, M., Abdoun, T., Elgamal, A., Zeghal, M., Ecemis, N., et al.: Laminar box system for 1-g physical modeling of liquefaction and lateral spreading. *Geotech. Test. J.* **32**(5), 438–449 (2009). DOI <https://doi.org/10.1520/GTJ102154>
76. Thornton, C.: Numerical simulations of deviatoric shear deformation of granular media. *Géotechnique* **50**(1), 43–53 (2000). DOI <https://doi.org/10.1680/geot.2000.50.1.43>
77. Tripathi, A., Khakhar, D.V.: Rheology of binary granular mixtures in the dense flow regime. *Physics of Fluids* **23**(11), 113302 (2011). DOI <https://doi.org/10.1063/1.3653276>
78. Tsuji, Y., Kawaguchi, T., Tanaka, T.: Discrete particle simulation of two-dimensional fluidized bed. *Powder Technol.* **77**(1), 79–87 (1993). DOI [https://doi.org/10.1016/0032-5910\(93\)85010-7](https://doi.org/10.1016/0032-5910(93)85010-7)
79. Xia, H., Hu, T.: Effects of saturation and back pressure on sand liquefaction. *J. Geotech. Eng.* **117**(9), 1347–1362 (1991). DOI [https://doi.org/10.1061/\(ASCE\)0733-9410\(1991\)117:9\(1347\)](https://doi.org/10.1061/(ASCE)0733-9410(1991)117:9(1347))
80. Yong, J.: Liquefaction resistance of sand in relation to P-wave velocity. *Géotechnique* **52**(4), 295–298 (2002). DOI <https://doi.org/10.1680/geot.2002.52.4.295>
81. Zhao, S., Zhao, J., Liang, W.: A thread-block-wise computational framework for large-scale hierarchical continuum-discrete modeling of granular media. *Int. J. Numer. Methods Eng.* **122**(2), 579–608 (2021). DOI <https://doi.org/10.1002/nme.6549>
82. Zienkiewicz, O.C., Bettess, P.: Soils and other saturated porous media under transient, dynamic conditions, general formulation and the validity of various simplifying assumptions. In: G.N. Pande, O.C. Zienkiewicz (eds.) *Soil Mechanics — Transient and Cyclic Loads*, pp. 1–16. John Wiley & Sons, Chichester (1982)